Chapter 11
Nonlinear DC-link PI Control for Airborne Wind Energy Systems During Pumping Mode

Korbinian Schechner, Florian Bauer and Christoph M. Hackl

Abstract During pumping mode, airborne wind energy systems are operated in two phases: A power generating reel-out phase and a power dissipating reel-in phase. The ground winch is connected via a DC-link voltage source converter to the grid. The control of its DC-link voltage is a challenging task due to the bidirectional power flow over the DC-link. Two PI controller designs are discussed: the classical PI controller with constant parameters and a nonlinear PI controller with online parameter adjustment. Based on a worst-case analysis of the physical properties, bounds on the constant parameters of the classical PI controller are derived leading to a conservative design to assure a stable operation also during the reel-in phase where the system dynamics are non-minimum phase. To overcome these limitations in the closed-loop bandwidth, a nonlinear PI controller is proposed which adjusts its parameters online. For controller design, the linearized system model is used and the controller parameters are computed via "online pole placement". Simulation results illustrate robustness, stability and improved control performance of the proposed nonlinear PI controller in comparison to the classical PI controller.

11.1 Introduction

Kites are a promising approach to harvest wind energy at high altitudes (see [5, 10, 14] and references therein): As shown in Fig. 11.1, the kite is tethered to a ground winch which is connected to an electric drive. Electric energy is generated in a

Korbinian Schechner · Christoph Hackl (✉)
Technische Universität München, Munich School of Engineering, Research group "Control of renewable energy systems (CRES)", Lichtenbergstr. 4a, 85748 Garching, Germany
e-mail: christoph.hackl@hm.edu

Florian Bauer
Technische Universität München, Institute for Electrical Drive Systems and Power Electronics, Arcisstr. 21, 80333 München, Germany

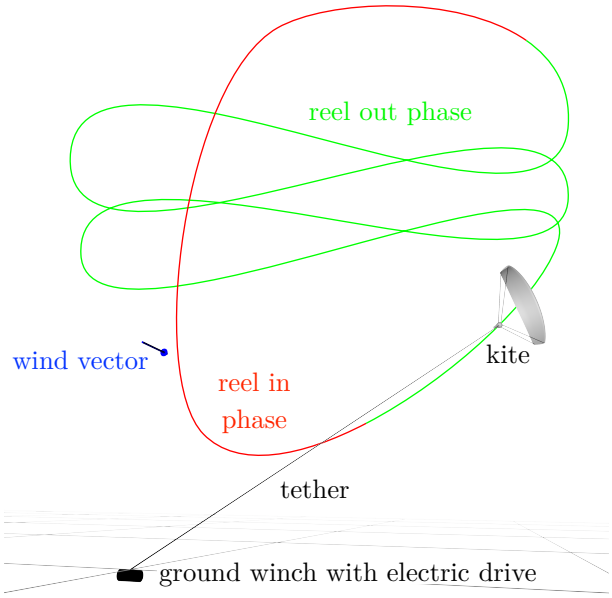

Fig. 11.1 Pumping mode power generation with a kite

pumping process: During the "reel-out phase", the kite is flown in fast crosswind motions like figure eights with a high lift force. The kite pulls the tether which is reeled out slowly. Energy is generated by operating the electric drive in generator mode, i.e. generative braking. In the "reel-in phase", the kite is flown in a low force position like the zenith, or is pitched down, and is reeled back in while only a fraction of the generated energy is dissipated by operating the winch drive in motor mode. Compared to conventional wind turbines, this technology promises to harvest wind energy at higher altitudes using less material. Hence, it promises to have a higher capacity factor, lower capital investments, and, therefore, a lower levelized cost of electricity.

Several challenges of this technology have to be solved for deployment in the power generation industry. In this chapter, we consider a ground winch with electric drive which is connected to the grid via a DC-link voltage source converter (or power converter). This topology allows for independent control of active and reactive power flow to and from the grid (bidirectional power flow). The DC-link dynamics are highly nonlinear and, during the reel-in phase (motor mode), are non-minimum phase which imposes a challenge on controller design. We discuss this challenge of DC-link voltage control under the influence of a highly fluctuating bi-directional power flow to and from the ground winch drive for a given reactive power demand by the grid operator.

From a control point of view, non-minimum phase systems are particularly interesting. In 1940 H.W. Bode was one of the first to discuss the phenomenon of

non-minimum phase systems (see [4]). For classical output feedback control, the closed-loop system bandwidth is drastically limited. High gains are not admissible and so a very conservative controller (mostly a proportional-integral (PI) controller) must be designed if constant controller parameters are used.

Although there exists a tremendous number of papers (over 8.000, see [7]) which deal with the subject of DC-link control, only quite few papers (see [6, 7, 12, 16–18, 23, 25, 27, 29–31]) do explicitly address the non-minimum phase behavior of the DC-link dynamics in their metadata (such as abstract, title or indexing words). There is quite a variety of proposed control strategies for the DC-link voltage control problem in power converters such as model predictive control strategies (see [8, 15, 28] and references therein), flatness-based methods, linearization-based or passivity-based approaches (see [11, 22] and references therein) or state-feedback controller designs (see [7, 21, 26]) to name a few. For airborne wind energy systems, DC-link control is conceptually explained in [2] and [1] in the context of grid integration of such renewable energy systems.

In this chapter (for first results see [3]), a nonlinear DC-link controller with online adjustment of its controller parameters for a grid-connected voltage source converter of an airborne wind energy system with bidirectional power flow (pumping mode operation) is proposed. In addition, we investigate the classical PI controller design with constant parameters. The focus on PI controllers is motivated by their widespread use in industry. The contributions of this chapter are:

- Precise problem formulation and detailed modeling of the nonlinear DC-link dynamics of a three-phase grid-connected voltage source converter,
- Linearization of the nonlinear DC-link dynamics around a general equilibrium,
- Illustration and physical explanation of the non-minimum phase property (which depends on the operation point),
- Description of classical PI controller design based on a physical worst-case analysis of the non-minimum phase behavior of the linearized system dynamics,
- Introduction of a nonlinear PI controller design where the controller parameters are continuously adjusted online with respect to the actual "operating point". To ease implementation, analytical expressions to adjust the controller parameters online are derived based on the physical properties of the system dynamics, and
- Simulation results to illustrate and compare the control performance of the classical and the proposed nonlinear PI controller design. To show realistic results, the simulation comprises nonlinear and realistic models of the voltage source converter with pulse width modulation, underlying current control loops and nonlinear power flow and nonlinear DC-link dynamics. Moreover, as realistic input to the simulation model, the measured bi-directional (mechanical) power flow of a real airborne wind energy demonstrator during pumping mode is used (see Fig. 11.2, Courtesy of Roland Schmehl, TU Delft).

We do not present a thorough stability analysis of the proposed nonlinear controller. However, as a proof of concept, the simulation results illustrate that the closed-loop system is stable and robust to (bounded) parameter uncertainties.

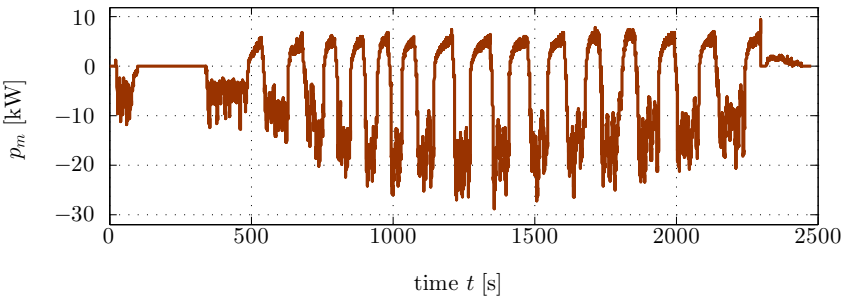

Fig. 11.2 Machine power $p_m(\cdot)$ measured by the TU Delft Kite Power group with their demonstrator on 23rd June 2012 kindly provided for our analysis. Negative is power generation (generator mode), positive is power demand (motor mode)

11.2 Problem Formulation

We consider a grid-connected power converter as shown in Fig. 11.3. It shares its DC-link with at least one electrical drive (electrical machine and voltage source inverter). The electrical drive is the actuator of the electrical drive train of the airborne wind energy (AWE) system which consists of the winch, the electrical machine (e.g. a permanent-magnet, reluctance or electrically-excited synchronous machine under four-quadrant control) and a voltage source inverter. The electrical drive converts mechanical power to electrical (machine[1]) power[2] $p_m\,[\mathrm{W}]$ which is exchanged with the DC-link via the DC-link power $p_{\mathrm{dc}}\,[\mathrm{W}]$ and the grid-connected converter via the grid-side converter output power $p_g\,[\mathrm{W}]$. During pumping mode (see Fig. 11.2), the machine power p_m changes its sign: During the reel-out phase, energy is generated (i.e. $p_m < 0$) and, during the reel-in phase, energy is dissipated (i.e. $p_m > 0$) in the ground winch drive system. Due to the DC-link with capacitance $C_{\mathrm{dc}}\,[\mathrm{F}]$, machine and grid side are electrically coupled via the electrical power flow over the DC-link (for more details see Sect. 11.3) but for an almost constant DC-link voltage $u_{\mathrm{dc}}\,[\mathrm{V}]$ both sides can be considered separately.

The grid-connected converter generates the voltages $\mathbf{u}_f^{abc} = (u_f^a, u_f^b, u_f^c)^\top\,[\mathrm{V}]^3$ which are applied to the RL-filter.[3] At the point of common coupling (PCC, i.e. the point of the grid connection), a current $\mathbf{i}_f^{abc} = (i_f^a, i_f^b, i_f^c)^\top\,[\mathrm{A}]^3$ will flow through the RL-filter with resistance $R_f\,[\Omega]$ and inductance $L_f\,[\mathrm{H}]$ into the balanced (ideal) grid with voltage $\mathbf{u}_g^{abc} = (u_g^a, u_g^b, u_g^c)^\top\,[\mathrm{V}]^3$. To control the power flow on the grid side, the power converter requires a sufficiently large (positive) and almost constant DC-link voltage $u_{\mathrm{dc}} \geq u_{\mathrm{dc,min}}$, where $u_{\mathrm{dc,min}} > 0\,[\mathrm{V}]$ is the required minimum DC-link volt-

[1] Actually, the electrical power $p_e = \eta p_m$ is exchanged with the power converter. But, for simplicity, we assume that the electrical winch drive system has an efficiency of one, i.e. $\eta = 1$. This simplification is justified, since in real world, a non-ideal efficiency $\eta < 1$ would simply scale down the electrical power but will hardly affect the dynamics of the DC-link system.

[2] For details on the nomenclature of this chapter see p. 274.

[3] Another common filter topology is a LCL-filter (see [24, Chap. 11]).

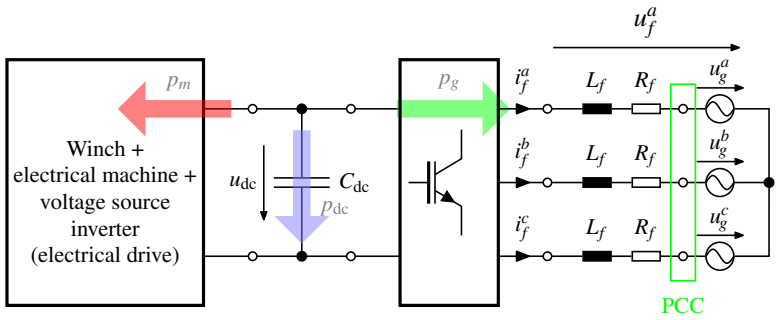

Fig. 11.3 Grid-connected converter with DC-link, filter and electrical drive

age for reasonable operation. The control objective is to achieve a stable set-point tracking of a given constant reference value $u_{\mathrm{dc,ref}} \geq u_{\mathrm{dc,min}} > 0$ for unknown and possibly bidirectional but bounded mechanical power flows $p_m(\cdot) \in \mathscr{L}^\infty(\mathbb{R}_{\geq 0};\mathbb{R})$.

We consider the reference currents $\mathbf{i}_{f,\mathrm{ref}}^{abc} = (i_{f,\mathrm{ref}}^a, i_{f,\mathrm{ref}}^b, i_{f,\mathrm{ref}}^c)^\top [\mathrm{A}]^3$ as control inputs, i.e. the underlying current control-loops (with decoupled controllers, voltage source converter and pulse width modulation or space vector modulation; for details see [9]) are already adequately designed. As feedback variables the currents $\mathbf{i}_f^{abc}$ and the DC-link voltage u_{dc} are available (full state-feedback).

11.3 Modeling and System Analysis of the Power Converter

For balanced three-phase systems (see Assumption (A.1) below), the system dynamics reduce to a two-phase system which is represented in a rotating $k = (d,q)$-reference frame or a fixed $s = (\alpha,\beta)$-reference frame instead of the (a,b,c)-reference frame. In general, for $\boldsymbol{\xi} \in \{\mathbf{u}_f, \mathbf{i}_f, \mathbf{i}_{f,\mathrm{ref}}, \mathbf{u}_g\}$, we write

$$\boldsymbol{\xi}^k(t) := \left(\xi^d(t), \xi^q(t)\right)^\top := \mathbf{T}_p(\phi_g(t))^{-1} \underbrace{\mathbf{T}_c \boldsymbol{\xi}^{abc}(t)}_{=:\boldsymbol{\xi}^s(t)}$$

where $\phi_g(t)\,[\mathrm{rad}]$ is the angle of the grid voltage,

$$\mathbf{T}_p(\phi_g) := \begin{bmatrix} \cos(\phi_g) & -\sin(\phi_g) \\ \sin(\phi_g) & \cos(\phi_g) \end{bmatrix}, \ \mathbf{J} := \begin{bmatrix} 0 & -1 \\ 1 & 0 \end{bmatrix} \ \text{and} \ \mathbf{T}_c := \frac{2}{3} \begin{bmatrix} 1 & -\frac{1}{2} & -\frac{1}{2} \\ 0 & \frac{\sqrt{3}}{2} & -\frac{\sqrt{3}}{2} \end{bmatrix} \quad (11.1)$$

are Park transformation matrix, rotation matrix (by $\frac{\pi}{2}$ counter-clock wise) and (simplified) Clarke transformation matrix, respectively (for details see [9, 24]). In the remainder of this chapter, we align the $k = (d,q)$-reference frame with the grid voltage ("grid voltage orientation"). For modeling, we impose the following assumptions:

Assumption (A.1) *The grid is balanced with constant angular frequency* $\omega_g > 0\,[\mathrm{rad/s}]$ *and the* $k=(d,q)$ *reference frame is aligned with the grid voltage having magnitude* $\widehat{u}_g > 0\,[\mathrm{V}]$*, i.e.* $u_g^a(t)+u_g^b(t)+u_g^c(t)=0$ *and*[4]

$$\forall t \geq 0\colon \qquad \mathbf{u}_g^k(t) = (u_g^d(t),\, u_g^q(t))^\top = (\widehat{u}_g,\, 0)^\top = \mathbf{T}_p(\phi_g(t))^{-1}\mathbf{T}_c\mathbf{u}_g^{abc}(t).$$

Assumption (A.2) *Power converter and DC-link are lossless (see Fig. 11.3), i.e.*

$$\forall t \geq 0\colon \qquad p_{\mathrm{dc}}(t) = -p_m(t) - p_g(t). \tag{11.2}$$

Assumption (A.3) *For current control-loop time constant* $T_{\mathrm{app}} > 0\,[\mathrm{s}]$*, the current dynamics are approximated by*

$$\frac{\mathrm{d}}{\mathrm{d}t}\mathbf{i}_f^k(t) = \tfrac{1}{T_{\mathrm{app}}}\big(-\mathbf{i}_f^k(t)+\mathbf{i}_{f,\mathrm{ref}}^k(t)\big), \quad \mathbf{i}_f^k(0) = \mathbf{i}_{f,0}^k := \mathbf{T}_p(\phi_{g,0})^{-1}\mathbf{T}_c\mathbf{i}_{f,0}^{abc} \in \mathbb{R}^2. \tag{11.3}$$

Assumption (A.4) *Reactive power reference and machine power are unknown but bounded, i.e.* $q_{\mathrm{pcc,ref}}(\cdot) \in \mathscr{L}^\infty(\mathbb{R}_{\geq 0};\mathbb{R})$ *and* $p_m(\cdot) \in \mathscr{L}^\infty(\mathbb{R}_{\geq 0};\mathbb{R})$*, respectively.*

Assumption (A.5) *The magnitude* $\widehat{u}_g$ *of the grid voltage is large compared to the voltage drop over the filter resistance, i.e.* $2R_f i_f^d(t) + \widehat{u}_g > 0$ *for all* $t \geq 0$*.*

Remark 11.1. For unbalanced (non-symmetric) grids, the situation becomes more difficult and positive, negative and zero sequence components must be considered (see [24]). For the symmetric case, the voltage orientation of the $k=(d,q)$ reference frame is achieved by the use of an adequate phase-locked loop algorithm (see [24, Chap. 8]). Although modern power converters have an efficiency up to 98 %, switching losses depend on the switching frequency. So Assumption (A.2) is a simplification. Assumption (A.3) is a standard assumption for current control-loops and holds for sufficiently high switching and current control frequencies [19, Sect. 13.4]. Assumption (A.4) is reasonable from a physical point of view. For most practical applications, we have $\widehat{u}_g \gg 1$ and $R_f \ll 1$, so Assumption (A.5) should hold. We will show that Assumption (A.5) is crucial for feasibility of any DC-link voltage controller.

11.3.1 Nonlinear DC-link Dynamics

By invoking Kirchhoff's current and voltage laws, the dynamics of the grid-side electrical circuit (as shown in Fig. 11.3) can be derived in the (a,b,c)-reference frame as follows

$$\mathbf{u}_f^{abc}(t) = R_f\mathbf{i}_f^{abc}(t) + L_f\frac{\mathrm{d}}{\mathrm{d}t}\mathbf{i}_f^{abc}(t) + \mathbf{u}_g^{abc}(t), \qquad \mathbf{i}_f^{abc}(0) = \mathbf{i}_{f,0}^{abc}. \tag{11.4}$$

[4] Note that $\mathbf{u}_f^k(t) = \mathbf{T}_p(\phi_g(t))^{-1}\mathbf{T}_c\mathbf{u}_f^{abc}(t)$ where $\phi_g(t) = \omega_g t + \phi_{g,0}$ for constant angular grid frequency $\omega_g > 0$ and initial angular position $\phi_{g,0} \in \mathbb{R}$.

Applying the (simplified) Clarke transformation as in Eq. (11.1) to Eq. (11.4) allows to rewrite the dynamics in the stationary $s=(\alpha,\beta)$-reference frame as follows

$$\begin{aligned}\mathbf{u}_f^s(t)=\mathbf{T}_c\mathbf{u}_f^{abc}(t) &\overset{(11.4)}{=} \mathbf{T}_c R_f \mathbf{i}_f^{abc}(t)+\mathbf{T}_c L_f\frac{\mathrm{d}}{\mathrm{d}t}\mathbf{i}_f^{abc}(t)+\mathbf{T}_c\mathbf{u}_g^{abc}(t)\\ &= R_f\mathbf{i}_f^s(t)+L_f\frac{\mathrm{d}}{\mathrm{d}t}\mathbf{i}_f^s(t)+\mathbf{u}_g^s(t),\qquad \mathbf{i}_f^s(0)=\mathbf{T}_c\mathbf{i}_{f,0}^{abc}. \quad (11.5)\end{aligned}$$

Then, in view of Assumption (A.1), utilizing the Park transformation as in Eq. (11.1) and the product rule[5] yield the system dynamics

$$\begin{aligned}\mathbf{u}_f^k(t) &= \mathbf{T}_p(\phi_g(t))^{-1}\mathbf{u}_f^s(t)\\ &\overset{(11.5)}{=} \mathbf{T}_p(\phi_g(t))^{-1}R_f\mathbf{i}_f^s(t)+\mathbf{T}_p(\phi_g(t))^{-1}L_f\frac{\mathrm{d}}{\mathrm{d}t}\big(\mathbf{T}_p(\phi_g(t))\mathbf{i}_f^k(t)\big)+\mathbf{T}_p(\phi_g(t))^{-1}\mathbf{u}_g^s(t)\\ &= R_f\mathbf{i}_f^k(t)+L_f\frac{\mathrm{d}}{\mathrm{d}t}\mathbf{i}_f^k(t)+\omega_g L_f\mathbf{J}\mathbf{i}_f^k(t)+\mathbf{u}_g^k(t) \quad (11.6)\end{aligned}$$

in the rotating $k=(d,q)$-reference frame (with grid voltage orientation). In view of Assumption (A.2), the power balance in Eq. (11.2) holds at the DC-link which, for

$$p_{\mathrm{dc}}(t)=u_{\mathrm{dc}}(t)C_{\mathrm{dc}}\tfrac{\mathrm{d}}{\mathrm{d}t}u_{\mathrm{dc}}(t)\quad\text{ and }\quad p_g(t)=\mathbf{u}_f^{abc}(t)^\top\mathbf{i}_f^{abc}(t)=\tfrac{3}{2}\mathbf{u}_f^k(t)^\top\mathbf{i}_f^k(t),$$

[24, Sect. 9.2] and, in view of Assumption (A.3), leads to the nonlinear DC-link dynamics in the rotating $k=(d,q)$-reference frame (for details see [9])

$$\begin{aligned}\tfrac{\mathrm{d}}{\mathrm{d}t}u_{\mathrm{dc}}(t) &\overset{(11.2)}{=} \tfrac{1}{C_{\mathrm{dc}}u_{\mathrm{dc}}(t)}\left[-p_m(t)-\tfrac{3}{2}\mathbf{u}_f^k(t)^\top\mathbf{i}_f^k(t)\right],\qquad u_{\mathrm{dc}}(0)=u_{\mathrm{dc},0}\\ &\overset{(11.6)}{=} \tfrac{3}{2C_{\mathrm{dc}}u_{\mathrm{dc}}(t)}\Bigg[-\tfrac{2}{3}p_m(t)-R_f\left\|\mathbf{i}_f^k(t)\right\|^2-L_f\mathbf{i}_f^k(t)\tfrac{\mathrm{d}}{\mathrm{d}t}\mathbf{i}_f^k(t)\\ &\qquad -\widehat{u}_g i_f^d(t)-\underbrace{\omega_g L_f\mathbf{i}_f^k(t)^\top\mathbf{J}^\top\mathbf{i}_f^k(t)}_{=0}\Bigg] \quad (11.7)\\ &\overset{(11.3)}{=} \tfrac{3}{2C_{\mathrm{dc}}u_{\mathrm{dc}}(t)}\Bigg[-\tfrac{2}{3}p_m(t)-\left(R_f-\tfrac{L_f}{T_{\mathrm{app}}}\right)\left\|\mathbf{i}_f^k(t)\right\|^2\\ &\qquad -\tfrac{L_f}{T_{\mathrm{app}}}\mathbf{i}_f^k(t)^\top\mathbf{i}_{f,\mathrm{ref}}^k(t)-\widehat{u}_g i_f^d(t)\Bigg] \quad (11.8)\end{aligned}$$

with initial value $u_{\mathrm{dc}}(0)=u_{\mathrm{dc},0}\geq u_{\mathrm{dc,min}}>0$, which is positive due to the flyback diodes in the power converter [20, Sect. 8.3].

The reactive power at the point of common coupling (PCC) is given by $q_{\mathrm{pcc}}(t)=-\frac{3}{2}\widehat{u}_g i_f^q(t)$ [24, Sect. 9.2] and the reactive power reference $q_{\mathrm{pcc,ref}}(\cdot)$ will be provided

[5] Note that $\frac{\mathrm{d}}{\mathrm{d}t}\mathbf{T}_p(\phi_g(t))=\omega_g\mathbf{T}_p(\phi_g(t))\mathbf{J}$ holds for all $t\geq 0$ and $\phi_g(t)=\omega_g t+\phi_{g,0}$.

by the grid operator. Hence, in view of Assumption (A.4), the current reference is

$$i_{f,\mathrm{ref}}^{q}(t) = -\tfrac{2\,q_{\mathrm{pcc,ref}}(t)}{3\,\widehat{u}_g}. \tag{11.9}$$

So, the q-component of the filter current is, for all $t \geq 0$, given by

$$|i_f^q(t)| = \left| \mathrm{e}^{-\frac{t}{T_{\mathrm{app}}}} i_{f,0}^{q} - \int_{t_0}^{t} \mathrm{e}^{-\frac{1}{T_{\mathrm{app}}}(t-\tau)} \tfrac{2q_{\mathrm{pcc,ref}}(\tau)}{3T_{\mathrm{app}}\widehat{u}_g} \right| \overset{(A.4)}{\leq} |i_{f,0}^{q}| + \tfrac{2\|q_{\mathrm{pcc,ref}}\|_\infty}{3\widehat{u}_g} \tag{11.10}$$

and can be regarded as time-varying but bounded disturbance to the DC-link dynamics given in Eq. (11.8). For the following, we define state vector, input and disturbance by

$$\mathbf{x} := \begin{pmatrix} x_1 \\ x_2 \end{pmatrix} := \begin{pmatrix} u_{\mathrm{dc}} \\ i_f^d \end{pmatrix},\ u := i_{f,\mathrm{ref}}^{d},\ d := \tfrac{2}{3}p_m + \left(R_f - \tfrac{L_f}{T_{\mathrm{app}}}\right)(i_f^q)^2 - \tfrac{2L_f}{3T_{\mathrm{app}}\widehat{u}_g} i_f^q q_{\mathrm{pcc,ref}} \tag{11.11}$$

(with i_f^q as in Eq. (11.10)), respectively. Note that, by Assumptions (A.4), $d(\cdot) \in \mathscr{L}^\infty(\mathbb{R}_{\geq 0};\mathbb{R})$ holds. The (reduced) system dynamics can be written in standard form as follows

$$\left.\begin{aligned} \tfrac{\mathrm{d}}{\mathrm{d}t}\mathbf{x}(t) &= \mathbf{f}(\mathbf{x}(t), u(t), d(t)), \qquad \mathbf{x}(0) = \begin{pmatrix} u_{\mathrm{dc},0} \\ i_{f,0}^{d} \end{pmatrix} \\ y(t) &= \underbrace{\begin{pmatrix} 1 & 0 \end{pmatrix}}_{=:\mathbf{c}^\top} \mathbf{x}(t) \end{aligned}\right\} \tag{11.12}$$

where

$$\begin{aligned} &\mathbf{f}\colon \mathbb{R}^2 \times \mathbb{R} \times \mathbb{R} \to \mathbb{R}^2,\ (\mathbf{x},u,d) \mapsto \mathbf{f}(\mathbf{x},u,d) := \\ &\begin{pmatrix} f_1(\mathbf{x},u,d) \\ f_2(\mathbf{x},u,d) \end{pmatrix} := \begin{pmatrix} \frac{3}{2C_{\mathrm{dc}}x_1}\left(-\left(R_f - \frac{L_f}{T_{\mathrm{app}}}\right)x_2^2 - \frac{L_f}{T_{\mathrm{app}}}x_2 u - \widehat{u}_g x_2 - d\right) \\ \frac{1}{T_{\mathrm{app}}}(-x_2 + u) \end{pmatrix}. \end{aligned} \tag{11.13}$$

11.3.2 Equilibrium and Linearization

For the following denote state, control input and disturbance at an equilibrium by

$$\left.\begin{aligned} \mathbf{x}^\star &:= (x_1^\star, x_2^\star)^\top = (u_{\mathrm{dc}}^\star, i_f^{d,\star})^\top \\ u^\star &:= i_{f,\mathrm{ref}}^{d,\star} \\ d^\star &:= \tfrac{2}{3}p_l^\star + \left(R_f - \tfrac{L_f}{T_{\mathrm{app}}}\right)(i_f^{q,\star})^2 - \tfrac{2L_f i_f^{q,\star}}{3T_{\mathrm{app}}\widehat{u}_g} q_{\mathrm{PCC,ref}}^\star \overset{(11.9)}{=} \tfrac{2}{3}p_l^\star + R_f (i_f^{q,\star})^2. \end{aligned}\right\} \tag{11.14}$$

At equilibrium given in Eqs. (11.14), the following must hold $\frac{\mathrm{d}}{\mathrm{d}t}\mathbf{x} = \mathbf{f}(\mathbf{x}^\star, u^\star, d^\star) = \mathbf{0}_2$, which gives

$$u^\star = x_2^\star \qquad \text{and} \qquad R_f (x_2^\star)^2 + \widehat{u}_g x_2^\star = -d^\star, \tag{11.15}$$

where the second condition in Eq. (11.15) has the solution(s)

$$x_2^\star = -\frac{\widehat{u}_g}{2R_f}\left(1 \mp \sqrt{1 - \frac{4d^\star R_f}{\widehat{u}_g^2}}\right).$$

Only, for $d^\star \leq \frac{\widehat{u}_g^2}{4R_f}$ (which holds since $\widehat{u}_g \gg 1$ and $R_f \ll 1$ in real world), the solution is physically meaningful (non-complex roots). By denoting the small signals by

$$\mathbf{x}_l := \mathbf{x} - \mathbf{x}^\star, \quad u_l := u - u^\star, \quad y_l := y - y^\star, \quad \text{and} \quad d_l := d - d^\star, \tag{11.16}$$

a linearization of system in Eqs. (11.12) around the equilibrium $(\mathbf{x}^\star, \mathbf{u}^\star, d^\star)$ yields

$$\left.\begin{aligned} \tfrac{\mathrm{d}}{\mathrm{d}t}\mathbf{x}_l(t) &= \mathbf{A}^\star \mathbf{x}_l(t) + \mathbf{b}^\star u_l(t) + \mathbf{b}_d^\star d_l(t) \\ y_l(t) &= \mathbf{c}^\top \mathbf{x}_l(t) \end{aligned}\right\} \tag{11.17}$$

where higher order terms are neglected and[6]

$$\mathbf{A}^\star := \left.\frac{\partial \mathbf{f}(\mathbf{x},u,d)}{\partial \mathbf{x}}\right|_{(\mathbf{x}^\star,u^\star,d^\star)} \overset{(11.15)}{=} \begin{bmatrix} 0 & \overbrace{\frac{3}{2C_{\mathrm{dc}}u_{\mathrm{dc}}^\star}\left(\left(\frac{L_f}{T_{\mathrm{app}}} - 2R_f\right) i_f^{d,\star} - \widehat{u}_g\right)}^{=:a_{12}^\star} \\ 0 & -\frac{1}{T_{\mathrm{app}}} \end{bmatrix} \in \mathbb{R}^{2\times 2}, \tag{11.18}$$

$$\mathbf{b}^\star := \left.\frac{\partial \mathbf{f}(\mathbf{x},u,d)}{\partial u}\right|_{(\mathbf{x}^\star,u^\star,d^\star)} = \begin{pmatrix} \overbrace{-\frac{3}{2C_{\mathrm{dc}}u_{\mathrm{dc}}^\star}\frac{L_f}{T_{\mathrm{app}}} i_f^{d,\star}}^{=:b_1^\star} \\ \frac{1}{T_{\mathrm{app}}} \end{pmatrix} \in \mathbb{R}^2 \tag{11.19}$$

and

$$\mathbf{b}_d^\star := \left.\frac{\partial \mathbf{f}(\mathbf{x},u,d)}{\partial d}\right|_{(\mathbf{x}^\star,u^\star,d^\star)} = \begin{pmatrix} -\frac{3}{2C_{\mathrm{dc}}u_{\mathrm{dc}}^\star} \\ 0 \end{pmatrix} \in \mathbb{R}^2. \tag{11.20}$$

In the following, for brevity, we use * as superscript to indicate that the corresponding variable (matrix, vector, coefficient) depends on the operation point (e.g. $\mathbf{A}^\star = \mathbf{A}^\star(\mathbf{x}^\star, u^\star, d^\star)$ or $a_{12}^\star = a_{12}^\star(\mathbf{x}^\star)$), whereas variables without * do not depend on the operation point as given in Eqs. (11.14).

[6] Note that $\left.\frac{\partial f_1(\mathbf{x},u,d)}{\partial x_1}\right|_{(\mathbf{x}^\star,u^\star,d^\star)} = -\frac{1}{x_1^\star}\underbrace{f_1(\mathbf{x}^\star,u^\star,d^\star)}_{=0} = 0.$

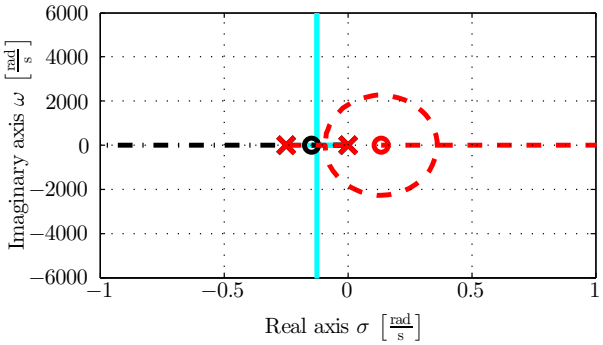

Fig. 11.4 Root locus of Eq. (11.21) for the cases (○: zero, ×: pole): —— $T_0^\star = 0$, - - - $T_0^\star > 0$ and ····· $T_0^\star < 0$ (non-minimum phase case)

11.3.3 Non-Minimum Phase Dynamics

To illustrate the non-minimum phase dynamics of the (linearized) system given in Eqs. (11.17) during reel-in phase, we compute the transfer function (for details see [9])

$$F_S(s) := \frac{y_l(s)}{u_l(s)} = \frac{(u_{\text{dc}} - u_{\text{dc}}^\star)(s)}{(i_{f,\text{ref}}^d - i_f^d)(s)} = \mathbf{c}^\top \left(s\mathbf{I}_2 - \mathbf{A}^\star\right)^{-1} \mathbf{b}^\star = -\frac{V_S^\star(1+sT_V^\star)}{s(1+sT_{\text{app}})}. \tag{11.21}$$

where system gain $V_S^\star\,[\text{V/A}]$ and numerator time constant $T_V^\star\,[\text{s}]$ depend on the current $i_f^{d,\star}$ and are defined as follows

$$\boxed{V_S^\star := V_S^\star(i_f^{d,\star}, u_{\text{dc}}^\star) := \frac{3(\widehat{u}_g + 2R_f i_f^{d,\star})}{2C_{\text{dc}} u_{\text{dc}}^\star} \quad \text{and} \quad T_V^\star := T_V^\star(i_f^{d,\star}) := \frac{L_f i_f^{d,\star}}{\widehat{u}_g + 2R_f i_f^{d,\star}}.} \tag{11.22}$$

For different operating points $(\mathbf{x}^\star, u^\star, d^\star)$, the numerator time constant $T_V^\star$ can either be zero, positive or negative (note that, in view of Assumption (A.5), we have $\widehat{u}_g + 2R_f i_f^{d,\star} > 0$). During the reel-in phase (motor mode), we have a zero in the right (unstable) complex half-plane, since power is drawn from the grid and transferred to the DC-link (see Fig. 11.3), i.e. $i_f^{d,\star} < 0$ and, hence, $T_V^\star < 0$: The system is *non-minimum phase*. In Fig. 11.4, the root loci of Eq. (11.21) are plotted for the three cases $T_V^\star = 0$, $T_V^\star > 0$ and $T_V^\star < 0$. If $T_V^\star < 0$, too large gains will render the closed-system unstable which necessitates a rather conservative controller design.

11.3.4 Physical Explanation of the Non-Minimum Phase Behavior

In this section, we will explain the non-minimum phase behavior from a physical point of view. In particular, we will discuss the often observed initially reversed system response due to step-like reference changes.

First note that the DC-link voltage is (normally) larger than the grid voltage amplitude, i.e. $u_{\mathrm{dc}} > \widehat{u}_g$. Hence, during the reel-in phase, the power converter operates as boost converter to transfer energy from the grid to the DC-link which requires that energy is stored in the filter inductance before it can be pushed into the DC-link. For our analysis, we will consider a time instant $t \geq 0$ with the following properties

$$\left.\begin{array}{ll} \text{(i)} & i_f^d(t) < 0 \ \text{(i.e. current flows from grid to DC-link),} \\ \text{(ii)} & p_m(t) > 0 \ \text{(i.e. reel-in phase, motor mode), and} \\ \text{(iii)} & \frac{\mathrm{d}}{\mathrm{d}t} i_f^q(t) = i_f^q(t) = 0 \ \text{(i.e. no reactive power).} \end{array}\right\} \tag{11.23}$$

For Eqs. (11.23), the nonlinear DC-link dynamics in Eq. (11.7) simplify to

$$\frac{\mathrm{d}}{\mathrm{d}t} u_{\mathrm{dc}}(t) = \underbrace{\frac{1}{u_{\mathrm{dc}}(t) C_{\mathrm{dc}}}}_{\substack{>0, \text{ see} \\ \text{Sect. 11.3.1}}} \left[\underbrace{-p_m(t)}_{\overset{(11.23)}{<} 0} \underbrace{-\tfrac{3}{2} R_f i_f^d(t)^2}_{<0} - \tfrac{3}{2} L_f i_f^d(t) \tfrac{\mathrm{d}}{\mathrm{d}t} i_f^d(t) \underbrace{-\tfrac{3}{2} \widehat{u}_g i_f^d(t)}_{\overset{(11.23)}{>} 0} \right]. \tag{11.24}$$

We will only consider the case of a positive DC-link voltage reference change, i.e.

$$u_{\mathrm{dc,ref}}(t) > u_{\mathrm{dc}}(t) \quad \Longrightarrow \quad i_{f,\mathrm{ref}}^d(t) < i_f^d(t) \overset{(11.23)}{<} 0 \quad \overset{(11.3)}{\Longrightarrow} \quad \tfrac{\mathrm{d}}{\mathrm{d}t} i_f^d(t) < 0. \tag{11.25}$$

The other case follows analogously. To (immediately) increase the DC-link voltage, $\frac{\mathrm{d}}{\mathrm{d}t} u_{\mathrm{dc}}(t) > 0$ must hold and, from Eq. (11.24), it follows that this is feasible if and only if the time derivative of magnetic energy (in the filter inductance) satisfies

$$\tfrac{3}{2} L_f i_f^d(t) \frac{\mathrm{d}}{\mathrm{d}t} i_f^d(t) < \big(\underbrace{-p_m(t)}_{\overset{(11.23)}{<} 0} \underbrace{-\tfrac{3}{2} R_f i_f^d(t)^2}_{<0} \underbrace{-\tfrac{3}{2} \widehat{u}_g i_f^d(t)}_{\overset{(11.23)}{>} 0} \big) =: \alpha(t). \tag{11.26}$$

There exist two scenarios when the DC-link voltage will initially decrease, i.e. the typical non-minimum phase behavior with initially reversed system response:

- (S_1) For a very large machine power $p_m(t) \gg 1$ (energy dissipation), we might have $\alpha(t) < 0$. Then, due to $i_f^d(t) < 0$ and $\frac{\mathrm{d}}{\mathrm{d}t} i_f^d(t) < 0$ in Eq. (11.25), the change in the magnetic energy $\frac{3}{2} L_f i_f^d(t) \frac{\mathrm{d}}{\mathrm{d}t} i_f^d(t)$ is positive which contradicts Eq. (11.26) and $u_{\mathrm{dc}}(\cdot)$ will decrease until $\alpha(\tau) > 0$ will change its sign at some $\tau > t \geq 0$.
- (S_2) For a small machine power $p_m(t) > 0$ and a large grid voltage $\widehat{u}_g \gg 1$, we might have $\alpha(t) > 0$. But very fast current dynamics in Eq. (11.3) might yield $\frac{3}{2} L_f i_f^d(t) \frac{\mathrm{d}}{\mathrm{d}t} i_f^d(t) \geq \alpha(t)$ which also contradicts Eq. (11.26) and leads to an initial

decrease of $u_{\mathrm{dc}}(\cdot)$ until Eq. (11.26) holds again for some $\tau > t \geq 0$ with $\alpha(\tau) > \alpha(t)$.

Note that such a time instant $\tau > t \geq 0$ does exist, since the active power drawn from the grid, i.e. $-\frac{3}{2}\widehat{u}_g i_f^d(t)$ in Eq. (11.26), will become larger and larger for more and more negative currents $i_f^d(\cdot)$ (as result of $\frac{\mathrm{d}}{\mathrm{d}t} i_f^d(t) < 0$).

Concluding, the non-minimum phase behavior of the DC-link voltage control problem arises from the change of the magnetic energy $\frac{3}{2} L_f i_f^d(t) \frac{\mathrm{d}}{\mathrm{d}t} i_f^d(t)$ in the filter inductance which might constrain the time derivative of the DC-link voltage for positive changes of the machine power (see Experiment (E_1) in Fig. 11.8 at $t = 0.2\,\mathrm{s}$) or for positive set-point changes of the DC-link reference voltage (see Experiment (E_3) in Fig. 11.12 at $t = 0.2\,\mathrm{s}$).

11.4 Classical DC-Link PI Controller Design

In this section, we discuss the classical PI controller design with *constant* controller parameters for the DC-link voltage set-point tracking problem.

For this classical approach the controller parameters are set after a reasonable tuning has been performed. The controller design is based on a (local) analysis of the linearized closed-loop system invoking the Hurwitz criterion. Applying a PI controller with transfer function

$$\boxed{F_{\mathrm{PI}}(s) = \frac{i_{f,\mathrm{ref}}^d(s)}{u_{\mathrm{dc,ref}}(s) - u_{\mathrm{dc}}(s)} = -V_R \frac{1+sT_n}{sT_n}}, \tag{11.27}$$

with controller gain $V_R\,[\mathrm{A/V}]$ and controller time constant $T_n\,[\mathrm{s}]$, to the (linearized) system in Eq. (11.21) yields the closed-loop transfer function

$$F_{\mathrm{CL,PI}}(s) = \frac{F_{\mathrm{PI}}(s)F_S(s)}{1+F_{\mathrm{PI}}(s)F_S(s)} = \frac{V_R V_S^\star \frac{(1+sT_n)\left(1+sT_V^\star\right)}{s^2 T_n\left(1+sT_{\mathrm{app}}\right)}}{1+V_R V_S^\star \frac{(1+sT_n)\left(1+sT_V^\star\right)}{s^2 T_n\left(1+sT_{\mathrm{app}}\right)}} = \frac{\frac{V_R V_S^\star}{T_{\mathrm{app}} T_n}(1+sT_n)\left(1+sT_V^\star\right)}{s^3 q_3^\star + s^2 q_2^\star + s q_1^\star + q_0^\star} =: \frac{N_{\mathrm{CL,PI}}(s)}{D_{\mathrm{CL,PI}}(s)} \tag{11.28}$$

with the coefficients

$$q_3^\star = 1, \quad q_2^\star = \frac{1}{T_{\mathrm{app}}} + \frac{V_R V_S^\star T_V^\star}{T_{\mathrm{app}}}, \quad q_1^\star = V_R V_S^\star \left(\frac{1}{T_{\mathrm{app}}} + \frac{T_V^\star}{T_n T_{\mathrm{app}}}\right), \quad q_0^\star = \frac{V_R V_S^\star}{T_n T_{\mathrm{app}}} \tag{11.29}$$

of the denominator polynomial $D_{\mathrm{CL,PI}}(s)$. Now, the controller parameters V_R and T_n have to be specified (and tuned) to guarantee a stable closed-loop system behavior for all three operation points $T_V^\star = 0$, $T_V^\star > 0$ and $T_V^\star < 0$.

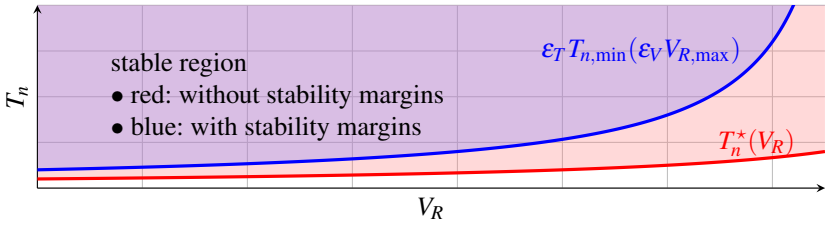

Fig. 11.5 Admissible region for controller gain V_R and controller time constant T_n to guarantee local stability (see sufficient conditions $(\mathbf{C}_1)$ and $(\mathbf{C}_2)$ in Eq. (11.30))

11.4.1 Local Stability Analysis Using the Hurwitz Criterion

In [9], the following two conditions for local stability were derived using the Hurwitz criterion:

$$(\mathbf{C}_1)\ 0 < V_R < \underbrace{\frac{1}{|T_V^\star| V_S^\star}}_{:=V_R^\star} \quad \text{and} \quad (\mathbf{C}_2)\ T_n > \underbrace{\frac{T_{\text{app}}}{1 - V_R V_S^\star |T_V^\star|} + |T_V^\star|}_{:=T_n^\star(V_R)} > 0. \tag{11.30}$$

These two conditions are *sufficient* and guarantee *local* stability in the sense that the Hurwitz criterion (i.e. $q_0^\star,\ q_1^\star,\ q_2^\star,\ q_3^\star > 0$ and $q_2^\star q_1^\star - q_3^\star q_0^\star > 0$ [13, Theorem 3.4.71]) is satisfied locally. The region for choosing admissible controller parameters to assure local stability is shown in Fig. 11.5.

Remark 11.2 (Controller sign). Note the minus sign of the PI controller in Eq. (11.27) which is crucial to compensate for the minus sign of the linearized system dynamics in Eq. (11.21).

11.4.2 Worst-Case Analysis

The upper and lower bounds in Eq. (11.30) on the controller gain V_R and the controller time constant T_n depend on the actual operating point in Eq. (11.14) (i.e., in particular, $i_f^{d,\star}$ and $u_{\text{dc}}^\star$). A worst-case analysis is beneficial such that the chosen controller parameters satisfy Eq. (11.30) for a wide range of different operation points. The goal of this section is to determine bounds $V_{R,\max}$ and $T_{n,\min}$ for the conditions in Eq. (11.30) such that the following holds for the complete operation range of the closed-loop system:

$$\begin{aligned} &\forall i_f^{d,\star} \in [i_{f,\min}^d,\, i_{f,\max}^d]\ \forall u_{\text{dc}}^\star \in [u_{\text{dc,min}}, u_{\text{dc,max}}]: \\ &\quad 0 < V_R < V_{R,\max} \le V_R^\star(i_f^{d,\star}, u_{\text{dc}}^\star) \quad \text{and} \quad T_n > T_{n,\min} \ge T_n^\star(i_f^{d,\star}) > 0. \end{aligned} \tag{11.31}$$

To derive the worst-case bounds on the controller parameters, the physical limits of the system in *steady state* are computed.

11.4.2.1 DC-Link Voltage Limits (in Steady State)

The steady state DC-link voltage is constrained by the lower (positive) limit

$$\boxed{u_{\mathrm{dc,min}} > \max\left\{\sqrt{\frac{4\omega_g^2 L_f^2 \widehat{u}_g^2}{R_f^2+\omega_g^2 L_f^2}}; \frac{3\sqrt{3}}{\pi}\widehat{u}_g\right\} > 0,} \tag{11.32}$$

which is due to the flyback diodes (which act as rectifier and, in continuous conduction mode, give the DC-link voltage $\frac{3\sqrt{3}}{\pi}\widehat{u}_g$, see [20, pp. 85-90]), and the upper (positive) limit

$$\boxed{u_{\mathrm{dc,max}} > u_{\mathrm{dc,min}} > 0} \tag{11.33}$$

which is set by the user to protect the physical system (e.g. capacitance or switches).

11.4.2.2 Current Limits (in Steady State)

To ease computation of the physical upper and lower limits on the current i_f^d, the derivation is shown for steady state, i.e. $\frac{\mathrm{d}}{\mathrm{d}t}(\cdot) = 0$, and for $i_f^q = 0$ (which gives a maximal/minimal i_f^d). For this case, the system dynamics of Eq. (11.6) simplify to

$$u_f^d = R_f i_f^d + \widehat{u}_g \qquad \text{and} \qquad u_f^q = \omega_g L_f i_f^d. \tag{11.34}$$

Moreover, for a regularly sampled, symmetrical pulse width modulation scheme, the maximal magnitude of the admissible voltage vector (see [20, pp. 658-720]) is

$$\|\mathbf{u}_f^k\| = \sqrt{(u_f^d)^2 + (u_f^q)^2} \leq \tfrac{u_{\mathrm{dc}}}{2},$$

which leads to the following inequality constraint

$$\left\|\mathbf{u}_f^k\right\|^2 - \tfrac{u_{\mathrm{dc}}^2}{4} \overset{(11.34)}{=} \left(R_f^2 + \omega_g^2 L_f^2\right)(i_f^d)^2 + 2R_f\widehat{u}_g i_f^d + \widehat{u}_g^2 - \tfrac{u_{\mathrm{dc}}^2}{4} \leq 0. \tag{11.35}$$

Solving Eq. (11.35) for i_f^d and inserting $u_{\mathrm{dc}} = u_{\mathrm{dc}}^\star$ gives the two solutions

$$i_f^{d,\star}(u_{\mathrm{dc}}^\star) := \frac{-R_f\widehat{u}_g \pm \sqrt{\left(R_f^2+\omega_g^2 L_f^2\right)\frac{(u_{\mathrm{dc}}^\star)^2}{4} - \omega_g^2 L_f^2 \widehat{u}_g^2}}{R_f^2+\omega_g^2 L_f^2}. \tag{11.36}$$

Considering the maximally admissible DC-link voltage, i.e. $u_{\mathrm{dc}}^\star = u_{\mathrm{dc,max}}$, allows to compute the upper (positive) current limit

$$\boxed{i_{f,\max}^{d} := \frac{-R_f\widehat{u}_g+\sqrt{\left(R_f^2+\omega_g^2L_f^2\right)\frac{(u_{\mathrm{dc,max}})^2}{4}-\omega_g^2L_f^2\widehat{u}_g^2}}{R_f^2+\omega_g^2L_f^2} > 0.} \tag{11.37}$$

and the lower (negative) current limit

$$\boxed{i_{f,\min}^{d} := \frac{-R_f\widehat{u}_g-\sqrt{\left(R_f^2+\omega_g^2L_f^2\right)\frac{(u_{\mathrm{dc,max}})^2}{4}-\omega_g^2L_f^2\widehat{u}_g^2}}{R_f^2+\omega_g^2L_f^2} < 0 \text{ and } |i_{f,\min}^{d}| > i_{f,\max}^{d}.} \tag{11.38}$$

11.4.2.3 Worst-Case Selection of Controller Gain V_R

To derive the upper limit $V_{R,\max}$ for the controller gain V_R, it is necessary to identify the minimal value of $V_R^\star$ which can be done as follows

$$\forall i_f^{d,\star} \in [i_{f,\min}^{d},\, i_{f,\max}^{d}]\ \forall u_{\mathrm{dc}}^\star \in [u_{\mathrm{dc,min}}, u_{\mathrm{dc,max}}]:$$
$$V_R^\star(u_{\mathrm{dc}}^\star) \overset{(11.22),(A.5)}{=} \frac{2C_{\mathrm{dc}}u_{\mathrm{dc}}^\star}{3L_f\left|i_f^{d,\star}\right|} \overset{(11.36)}{=} \frac{2C_{\mathrm{dc}}\left(R_f^2+\omega_g^2L_f^2\right)u_{\mathrm{dc}}^\star}{3L_f\left(R_f\widehat{u}_g+\sqrt{\left(R_f^2+\omega_g^2L_f^2\right)\frac{(u_{\mathrm{dc}}^\star)^2}{4}-\omega_g^2L_f^2\widehat{u}_g^2}\right)} > 0. \tag{11.39}$$

To characterize the curve $V_R^\star(\cdot)$, its derivative with respect to $u_{\mathrm{dc}}^\star$ is computed

$$\frac{\mathrm{d}}{\mathrm{d}u_{\mathrm{dc}}^\star}V_R^\star(u_{\mathrm{dc}}^\star) = \frac{2C_{\mathrm{dc}}\left(R_f^2+\omega_g^2L_f^2\right)}{2L_f\left(R_f\widehat{u}_g+\sqrt{\left(R_f^2+\omega_g^2L_f^2\right)\frac{(u_{\mathrm{dc}}^\star)^2}{4}-\omega_g^2L_f^2\widehat{u}_g^2}\right)^2}\cdot$$
$$\cdot\left[R_f\widehat{u}_g+\sqrt{\left(R_f^2+\omega_g^2L_f^2\right)\frac{(u_{\mathrm{dc}}^\star)^2}{4}-\omega_g^2L_f^2\widehat{u}_g^2}-\frac{R_f^2+\omega_g^2L_f^2}{4\sqrt{\left(R_f^2+\omega_g^2L_f^2\right)\frac{(u_{\mathrm{dc}}^\star)^2}{4}-\omega_g^2L_f^2\widehat{u}_g^2}}\,{u_{\mathrm{dc}}^\star}^2\right], \tag{11.40}$$

which shows that $V_R^\star(\cdot)$ is a monotonically decreasing function until its minimum is reached at (see Fig. 11.6)

$$u_{\mathrm{dc}}^\star = u_{\mathrm{dc}}^{\mathrm{opt}} := \sqrt{\frac{4\omega_g^2L_f^2\widehat{u}_g^2}{R_f^2+\omega_g^2L_f^2}\left(\frac{\omega_g^2L_f^2}{R_f^2}+1\right)},$$

since the following holds true

$$\forall\, u_{\mathrm{dc}}^\star \in \left(u_{\mathrm{dc,min}}, u_{\mathrm{dc}}^{\mathrm{opt}}\right): \qquad \frac{\mathrm{d}}{\mathrm{d}u_{\mathrm{dc}}^\star}V_R^\star(u_{\mathrm{dc}}^\star) < 0. \tag{11.41}$$

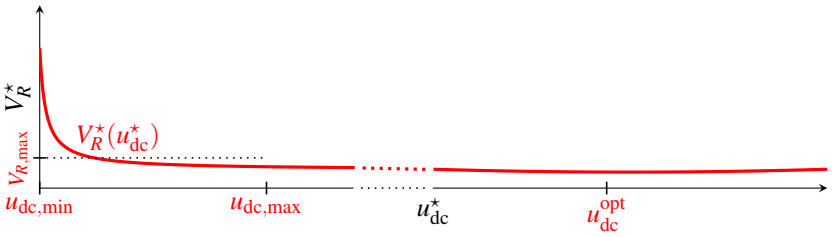

Fig. 11.6 Evolution of the function $u_{\mathrm{dc}}^\star \mapsto V_R^\star(u_{\mathrm{dc}}^\star)$ for $u_{\mathrm{dc}}^\star \geq u_{\mathrm{dc,min}}$

Note that $u_{\mathrm{dc,max}} \leq u_{\mathrm{dc}}^\star < u_{\mathrm{dc}}^{\mathrm{opt}}$ is *not* feasible, hence the minimum of $V_R^\star(\cdot)$ on the admissible interval $[u_{\mathrm{dc,min}}, u_{\mathrm{dc,max}}]$ is given by

$$V_R^\star(u_{\mathrm{dc,max}}) = \frac{2C_{\mathrm{dc}}\left(R_f^2+\omega_g^2 L_f^2\right)u_{\mathrm{dc,max}}}{3L_f\left(R_f\widehat{u}_g+\sqrt{\left(R_f^2+\omega_g^2L_f^2\right)\frac{(u_{\mathrm{dc,max}})^2}{4}-\omega_g^2L_f^2\widehat{u}_g^2}\right)} \overset{(11.38)}{=} \boxed{\frac{2C_{\mathrm{dc}}u_{\mathrm{dc,max}}}{3L_f\left|i_{f,\min}^d\right|} =: V_{R,\max},} \tag{11.42}$$

which represents a worst-case upper limit for the choice of the controller gain V_R of the *classical* PI controller in Eq. (11.27) with constant parameters. To satisfy the inequality in Eq. (11.31), we introduce a safety margin ε_V and choose the controller gain as follows

$$\boxed{V_R = \varepsilon_V V_{R,\max} \qquad \text{with} \qquad 0 < \varepsilon_V < 1.} \tag{11.43}$$

Remark 11.3 (Simplified worst case analysis). Note that a simplified worst case analysis yields

$$V_R^\star \;=\; \frac{1}{\left|T_V^\star\right|\left|V_S^\star\right|} \overset{(11.22),(A.5)}{=} \frac{2C_{\mathrm{dc}}u_{\mathrm{dc}}^\star}{3L_f\left|i_f^{d,\star}\right|} \overset{(11.38)}{\geq} \frac{2C_{\mathrm{dc}}u_{\mathrm{dc,min}}}{3L_f\left|i_{f,\min}^d\right|} =: \widetilde{V}_{R,\max}, \tag{11.44}$$

(i.e. using $u_{\mathrm{dc,min}}$ in the nominator instead of $u_{\mathrm{dc,max}}$) which gives even a more conservative upper bound on the PI controller gain V_R. For the simulated system in Sect. 11.6, this would cause a reduction of $V_{R,\max}$ by 37.5 % and, hence, an even more conservative controller design.

11.4.2.4 Worst-Case Selection of Controller Time Constant T_n

To select the controller time constant T_n as requested in Eq. (11.31), we need to derive the lower bound $T_{n,\min}$. Straight-forward calculations show that the following holds for all $i_f^{d,\star} \in [i_{f,\min}^d, i_{f,\max}^d]$ and for all $u_{\mathrm{dc}}^\star \in [u_{\mathrm{dc,min}}, u_{\mathrm{dc,max}}]$

$$T_n^\star \overset{(11.30)}{=} \frac{T_{\text{app}}}{1-V_R V_S^\star |T_V^\star|} + |T_V^\star| \overset{(11.30),(11.22)}{=} \frac{T_{\text{app}}}{1-\frac{V_R}{V_R^\star}} + \left| \frac{L_f i_f^{d,\star}}{\widehat{u}_g + 2R_f i_f^{d,\star}} \right|$$
$$\overset{(11.39)}{\leq} \frac{T_{\text{app}}}{1-\frac{V_R}{V_{R,\max}}} + \frac{L_f |i_f^{d,\star}|}{\widehat{u}_g - 2R_f |i_f^{d,\star}|} \overset{(11.38),(11.43)}{\leq} \boxed{\frac{T_{\text{app}}}{1-\varepsilon_V} + \frac{L_f |i_{f,\min}^d|}{\widehat{u}_g - 2R_f |i_{f,\min}^d|} =: T_{n,\min}}. \tag{11.45}$$

Now, for any stability margin $\varepsilon_T > 1$, we choose the controller time constant to

$$\boxed{T_n = \varepsilon_T T_{n,\min} > T_{n,\min} \geq T_n^\star(V_R) \qquad \text{with} \qquad \varepsilon_T > 1,} \tag{11.46}$$

and, therefore, will assure that Eq. (11.30) holds true.

11.5 Nonlinear DC-link PI Controller Design

Due to the possible non-minimum phase behavior of the DC-link dynamics and its *constant* controller parameters, the *classical* PI controller must be tuned in a very conservative fashion (recall Sect. 11.4.2) which leads to a very slow closed-loop system response for most operation points. In this section, we propose a nonlinear PI controller design which instantaneously adjusts its controller parameters to an (approximate) actual operation point ("online parameter adjustment"). The nonlinear controller has the following state space representation

$$\left.\begin{aligned} \tfrac{\mathrm{d}}{\mathrm{d}t} x_i(t) &= u_{\text{dc,ref}}(t) - u_{\text{dc}}(t)\,, & x_i(0) &= 0 \\ i_{f,\text{ref}}^d(t) &= V_R(i_f^d, u_{\text{dc}})\big(u_{\text{dc,ref}}(t) - u_{\text{dc}}(t)\big) + \tfrac{V_R(i_f^d,u_{\text{dc}})}{T_n(i_f^d,u_{\text{dc}})} x_i(t) \end{aligned}\right\} \tag{11.47}$$

and requires feedback of the actual d-component $i_f^d(t)$ of the filter current and the DC-link voltage $u_{\text{dc}}(t)$ (both are measured and, therefore, available for feedback).

For controller tuning, we specify a desired (local) closed-loop system response via a given Hurwitz polynomial and implement an "online pole placement" strategy to adjust the controller parameters online. Recalling the system order of the closed-loop system in Eq. (11.28), *three* poles have to be specified. More precisely, there is one *real* pole $\lambda_1 \in \mathbb{R}$ and a (possibly) *conjugate-complex* pole pair $\lambda_R \pm \imath\lambda_I \in \mathbb{C}$ which defines the desired closed-loop system polynomial

$$D_{\text{CL,PI}}^{\text{desired}}(s) := (s-\lambda_1)\,(s-\lambda_R-\imath\lambda_I)\,(s-\lambda_R+\imath\lambda_I) = s^3 p_3^\star + s^2 p_2^\star + s p_1^\star + p_0^\star \tag{11.48}$$

with coefficients

$$p_3^\star = 1, \quad p_2^\star = -2\lambda_R - \lambda_1, \quad p_1^\star = \lambda_R^2 + \lambda_I^2 + 2\lambda_1\lambda_R, \quad p_0^\star = -\lambda_1(\lambda_R^2 + \lambda_I^2). \tag{11.49}$$

Clearly, the desired polynomial in Eq. (11.48) must be a Hurwitz polynomial which is satisfied if and only if $\lambda_1 < 0$ and $\lambda_R < 0$ or $p_0^\star, p_1^\star, p_2^\star, p_3^\star > 0$ and $p_1^\star p_2^\star - p_3^\star p_0^\star > 0$ hold true. Important to note that, due to the use of a PI controller, we only have *two* design parameters (i.e. V_R and T_n) and, so, the problem is under-determined. Therefore, we will only specify (or fix) λ_R and λ_I and leave λ_1 free. It will depend on λ_R, λ_I, V_R and T_n and must be negative which has to be assured by an appropriate choice of λ_R and λ_I.

11.5.1 Pole Placement

Comparing the coefficients of the desired polynomial $D_{\mathrm{CL,PI}}^{\mathrm{desired}}(s)$ in Eq. (11.48) and the denominator polynomial $D_{\mathrm{CL,PI}}(s)$ of the linearized closed-loop system dynamics in Eq. (11.28) allows to solve for the controller parameters V_R and T_n and for the free pole λ_1 as follows (details are omitted)

$$\begin{aligned} V_R &= -\frac{2\lambda_R + T_V^\star\lambda_I^2 + T_V^\star\lambda_R^2 - T_{\mathrm{app}}\lambda_I^2 + 3T_{\mathrm{app}}\lambda_R^2 + 2T_V^\star T_{\mathrm{app}}\lambda_R^3 + 2T_V^\star T_{\mathrm{app}}\lambda_I^2\lambda_R}{V_S^\star\left((T_V^\star)^2\lambda_R^2 + (T_V^\star)^2\lambda_I^2 + 2T_V^\star\lambda_R + 1\right)} \\ &= -\frac{2\lambda_R\left(T_V^\star(\lambda_R^2+\lambda_I^2) + 2\lambda_R + \frac{1}{T_{\mathrm{app}}}\right) + \left(\frac{T_V^\star}{T_{\mathrm{app}}} - 1\right)\left(\lambda_R^2+\lambda_I^2\right)}{\frac{V_S^\star}{T_{\mathrm{app}}}\left((T_V^\star)^2\left(\lambda_R^2+\lambda_I^2\right) + 2T_V^\star\lambda_R + 1\right)}, \end{aligned} \tag{11.50}$$

$$\begin{aligned} T_n &= -\frac{2\lambda_R + T_V^\star\lambda_I^2 + T_V^\star\lambda_R^2 - T_{\mathrm{app}}\lambda_I^2 + 3T_{\mathrm{app}}\lambda_R^2 + 2T_V^\star T_{\mathrm{app}}\lambda_R^3 + 2T_V^\star T_{\mathrm{app}}\lambda_I^2\lambda_R}{\left(\lambda_R^2+\lambda_I^2\right)\left(T_V^\star T_{\mathrm{app}}\lambda_I^2 + T_V^\star T_{\mathrm{app}}\lambda_R^2 + 2T_{\mathrm{app}}\lambda_R + 1\right)} \\ &= -\frac{2\lambda_R\left(T_V^\star(\lambda_R^2+\lambda_I^2) + 2\lambda_R + \frac{1}{T_{\mathrm{app}}}\right) + \left(\frac{T_V^\star}{T_{\mathrm{app}}} - 1\right)\left(\lambda_R^2+\lambda_I^2\right)}{\left(\lambda_R^2+\lambda_I^2\right)\left(T_V^\star(\lambda_R^2+\lambda_I^2) + 2\lambda_R + \frac{1}{T_{\mathrm{app}}}\right)} \end{aligned} \tag{11.51}$$

and

$$\lambda_1 = -\frac{T_V^\star\left(\lambda_R^2+\lambda_I^2\right) + 2\lambda_R + \frac{1}{T_{\mathrm{app}}}}{(T_V^\star)^2\left(\lambda_R^2+\lambda_I^2\right) + 2T_V^\star\lambda_R + 1}. \tag{11.52}$$

Remark 11.4. Solving for λ_R or λ_I (so one of those is free) instead of λ_1 would yield an infinite closed-loop pole or an infinite controller gain if $T_V^\star = 0$. Therefore, λ_1 is considered as free pole.

11.5.2 Sufficient Condition for (Local) Stability

For a stable behavior of the closed-loop system in Eq. (11.28), the real parts of all poles must be negative, i.e. $\lambda_1 < 0$ and $\lambda_R < 0$. Clearly, λ_R can be chosen negative, but value and sign of λ_1 depend on the time constant $T_V^\star$ of the linearized system in Eq. (11.21), the time constant T_{app} of the converter, and the real pole λ_R and the imaginary part λ_I of the conjugate-complex pole pair. Moreover, it has to be assured that the *varying* controller parameters $V_R = V_R(T_V^\star, V_S^\star)$ and $T_n = T_n(T_V^\star)$ will remain positive over the complete operation range (i.e. $T_V^\star = 0$, $T_V^\star > 0$ and $T_V^\star < 0$).

11.5.2.1 Assuring a Negative Real Pole λ_1

To assure that λ_1 in Eq. (11.52) is negative, we will derive bounds on the choices of $\lambda_R < 0$ and $\lambda_I \in \mathbb{R}$. First note that, we may rewrite the real pole as follows

$$\lambda_1 = -\frac{T_V^\star\left(\lambda_R^2+\lambda_I^2\right)+2\lambda_R+\frac{1}{T_{\text{app}}}}{(T_V^\star)^2\left(\lambda_R^2+\lambda_I^2\right)+2T_V^\star\lambda_R+1} =: -\frac{N_{\lambda_1}(T_V^\star)}{D_{\lambda_1}(T_V^\star)} \tag{11.53}$$

in compact form. Analyzing the denominator yields

$$\begin{aligned} D_{\lambda_1}(T_V^\star) \;&:=\; (T_V^\star)^2\left(\lambda_R^2+\lambda_I^2\right)+2T_V^\star\lambda_R+1 \\ &=\; \begin{cases} 1 & T_V^\star = 0 \\ (T_V^\star)^2\left(\lambda_R+\frac{1}{T_V^\star}\right)^2+\lambda_I^2(T_V^\star)^2, & T_V^\star \neq 0 \end{cases} \\ \iff \quad & \forall T_V^\star \in \mathbb{R}: \qquad D_{\lambda_1}(T_V^\star) > 0, \end{aligned} \tag{11.54}$$

which shows that the denominator D_{λ_1} is positive over the whole operation range. Hence, to achieve $\lambda_1 < 0$, the numerator of Eq. (11.53) must also be positive, i.e. $N_{\lambda_1}(T_V^\star) > 0$ for all operation points $T_V^\star = 0$, $T_V^\star > 0$, and $T_V^\star < 0$. The numerator can be written as

$$\begin{aligned} N_{\lambda_1}(T_V^\star) &:= T_V^\star(\lambda_R^2+\lambda_I^2)+2\lambda_R+\tfrac{1}{T_{\text{app}}} \\ &= \begin{cases} 2\lambda_R+\frac{1}{T_{\text{app}}} & T_V^\star = 0 \\ T_V^\star\left(\lambda_R+\frac{1}{T_V^\star}\right)^2+T_V^\star\lambda_I^2-\frac{1}{T_V^\star}+\frac{1}{T_{\text{app}}}, & T_V^\star \neq 0, \end{cases} \end{aligned} \tag{11.55}$$

which might change its sign with $T_V^\star$ and the choices of λ_R and λ_I. To check the sign of numerator N_{λ_1}, the three following cases have to be investigated to derive bounds on λ_R and λ_I, respectively:

- Case $T_V^\star = 0$:

$$N_{\lambda_1} \overset{(11.52)}{=} 2\lambda_R+\tfrac{1}{T_{\text{app}}} > 0 \quad \Longleftarrow \quad \lambda_R > -\tfrac{1}{2T_{\text{app}}} \tag{11.56}$$

- Case $T_V^\star > 0$:

$$N_{\lambda_1} \overset{(11.52)}{=} \underbrace{T_V^\star \lambda_I^2}_{>0} + \underbrace{T_V^\star \lambda_R^2}_{>0} + 2\lambda_R + \tfrac{1}{T_{\text{app}}} > 0 \quad \Longleftarrow \quad \lambda_R > -\tfrac{1}{2T_{\text{app}}} \tag{11.57}$$

- Case $T_V^\star < 0$:

$$N_{\lambda_1} = T_V^\star \left(\lambda_R + \tfrac{1}{T_V^\star}\right)^2 + T_V^\star \lambda_I^2 - \tfrac{1}{T_V^\star} + \tfrac{1}{T_{\text{app}}} > 0$$

$$\Longleftarrow \quad |\lambda_R| > -\tfrac{1}{T_V^\star} \pm \sqrt{-\lambda_I^2 + \tfrac{1}{(T_V^\star)^2} - \tfrac{1}{T_V^\star T_{\text{app}}}} \text{ and } |\lambda_I| < \sqrt{\tfrac{1}{T_{\text{app}}|T_V^\star|}} \tag{11.58}$$

Evaluating and combining the results above and imposing the necessary condition $\lambda_R < 0$, we obtain the following sufficient condition

$$\boxed{\begin{aligned} &\max\left\{-\tfrac{1}{T_V^\star} - \sqrt{-\lambda_I^2 + \tfrac{1}{(T_V^\star)^2} - \tfrac{1}{T_V^\star T_{\text{app}}}}, -\tfrac{1}{2T_{\text{app}}}\right\} < \lambda_R < 0 \text{ and } |\lambda_I| < \sqrt{\tfrac{1}{T_{\text{app}}|T_V^\star|}} \\ &\qquad \Longrightarrow \quad \forall T_V^\star \in \mathbb{R}: \quad N_{\lambda_1}(T_V^\star) > 0 \quad \text{and} \quad D_{\lambda_1}(T_V^\star) > 0 \\ &\qquad \Longrightarrow \quad \forall T_V^\star \in \mathbb{R}: \quad \lambda_1 = -\tfrac{N_{\lambda_1}(T_V^\star)}{D_{\lambda_1}(T_V^\star)} < 0. \end{aligned}} \tag{11.59}$$

which assures local stability of the closed-loop system in Eq. (11.28).

Remark 11.5 (Comments on stability). Clearly, the nonlinear PI controller design is based on the linearized system in Eq. (11.17), hence pole placement will only hold locally. The drawback of a local result, we try to overcome by online adjustment of the controller parameters ("online pole placement"). However, by online adjustment, the controller parameters in Eq. (11.60) and in Eq. (11.61) of the linearized closed-loop system in Eq. (11.28) become "time-varying" or, more precisely, nonlinear. So global stability can not be deduced by checking negativity of the real parts of the poles of the linearized closed-loop system in Eq. (11.28).

11.5.2.2 Assuring Positive Controller Parameters

In addition to conditions in Eqs. (11.59), we check whether the controller parameters will remain positive over the whole operation range (otherwise positive feedback might endanger stability). First note that, by invoking N_{λ_1} as in Eq. (11.55) and D_{λ_1} as in Eq. (11.54), we may rewrite the controller parameters as follows

$$V_R = -\frac{2\lambda_R N_{\lambda_1}(T_V^\star) + \left(\frac{T_V^\star}{T_{\text{app}}} - 1\right)\left(\lambda_R^2 + \lambda_I^2\right)}{\frac{V_S^\star}{T_{\text{app}}} D_{\lambda_1}(T_V^\star)} \quad \text{and} \quad T_n = -\frac{2\lambda_R N_{\lambda_1}(T_V^\star) + \left(\frac{T_V^\star}{T_{\text{app}}} - 1\right)\left(\lambda_R^2 + \lambda_I^2\right)}{\left(\lambda_R^2 + \lambda_I^2\right) N_{\lambda_1}(T_V^\star)}.$$

In view of the sufficient conditions in Eqs. (11.59) for local stability and the additional but *physically reasonable* assumption:

Assumption (A.6) *For the whole operation range, the following holds true*

$$\forall i_f^{d,\star} \leq i_{f,\max}^d: \qquad T_V^\star(i_f^{d,\star}) < T_{\text{app}} \quad \Longleftrightarrow \quad \frac{T_V^\star(i_f^{d,\star})}{T_{\text{app}}} < 1,$$

it is easy to see that the numerators are negative and the denominators are positive, i.e. $2\lambda_R N_{\lambda_1}(T_V^\star) + \left(\frac{T_V^\star}{T_{\text{app}}} - 1\right)\left(\lambda_R^2 + \lambda_I^2\right) < 0, V_S^\star D_{\lambda_1}(T_V^\star) > 0$ and $\left(\lambda_R^2 + \lambda_I^2\right) N_{\lambda_1}(T_V^\star) > 0$ for all $T_V^\star \in \mathbb{R}$, which implies positivity of the controller parameters, i.e. $V_R(T_V^\star) > 0$ and $T_n(T_V^\star) > 0$ for all $T_V^\star \in \mathbb{R}$.

11.5.3 Online Adjustment of the Controller Parameters

This far the controller design was based on the linearized closed-loop dynamics assuming that an equilibrium exists. For implementation and online parameter adjustment the actual d-component current $i_f^d(t)$ and the actual DC-link voltage $u_{\text{dc}}(t)$ measurements will be used. Using the approximations

$$V_S^\star(i_f^d, u_{\text{dc}}) = \frac{3(\widehat{u}_g + 2R_f i_f^d)}{2C_{\text{dc}} u_{\text{dc}}} \approx V_S^\star(i_f^{d,\star}, u_{\text{dc}}^\star) \quad \text{and} \quad T_V^\star(i_f^d) \approx T_V^\star(i_f^{d,\star}) := \frac{L_f i_f^d}{\widehat{u}_g + 2R_f i_f^d}$$

the controller parameters become functions of the measured values as follows

$$\boxed{V_R(i_f^d(t), u_{\text{dc}}(t)) = -\frac{2\lambda_R\left(T_V^\star(i_f^d(t))(\lambda_R^2+\lambda_I^2) + 2\lambda_R + \frac{1}{T_{\text{app}}}\right) + \left(\frac{T_V^\star(i_f^d(t))}{T_{\text{app}}} - 1\right)\left(\lambda_R^2+\lambda_I^2\right)}{\frac{V_S^\star(i_f^d(t), u_{\text{dc}}(t))}{T_{\text{app}}}\left((T_V^\star)^2\left(\lambda_R^2+\lambda_I^2\right) + 2T_V^\star\lambda_R + 1\right)}} \tag{11.60}$$

and

$$\boxed{T_n(i_f^d(t)) = -\frac{2\lambda_R\left(T_V^\star(i_f^d(t))(\lambda_R^2+\lambda_I^2) + 2\lambda_R + \frac{1}{T_{\text{app}}}\right) + \left(\frac{T_V^\star(i_f^d(t))}{T_{\text{app}}} - 1\right)\left(\lambda_R^2+\lambda_I^2\right)}{\left(\lambda_R^2+\lambda_I^2\right)\left(T_V^\star(i_f^d(t))(\lambda_R^2+\lambda_I^2) + 2\lambda_R + \frac{1}{T_{\text{app}}}\right)}}. \tag{11.61}$$

Note that the integrator time "constant" $T_n(i_f^d(t))$ does not depend on $u_{\text{dc}}(t)$.

11.6 Simulation Results

In this section, the overall grid-connected voltage source power converter (including switching behavior, pulse width modulation underlying current control-loops) with the *classical* and the *nonlinear* DC-link PI controllers is implemented using Malab/Simulink. The goal is to investigate and illustrate (i) closed-loop system sta-

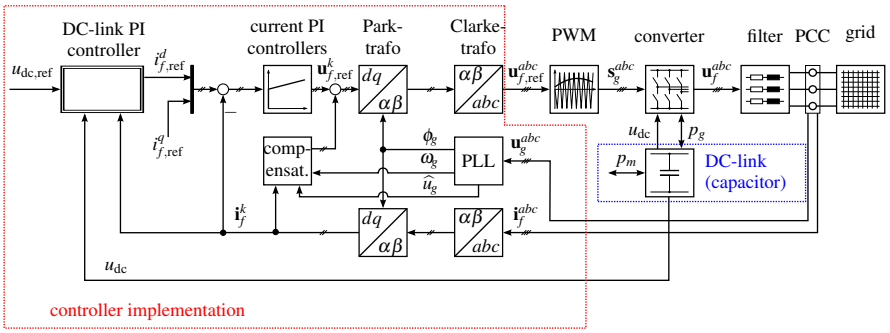

Fig. 11.7 Block diagram of the implementation of the overall DC-link control system with underlying current control-loops, switching behavior of the converter, pulse width modulation (PWM), and phase-locked loop (PLL) for grid synchronization. More details can be found in [9] (with similar notation) or [24, Chap. 9]

bility, (ii) control performance of the controllers and (iii) impact of parameter uncertainties on the control performance of the nonlinear PI controller.

11.6.1 Implementation

Fig. 11.7 shows the block diagram of the implementation of controller and DC-link system in Matlab/Simulink. Filter and grid are implemented as three-phase systems in the (a,b,c)-reference frame (instead of Eq. (11.6), for details see [9]). The DC-link dynamics are as in Eq. (11.2). For given filter voltage reference $\mathbf{u}_{f,\mathrm{ref}}^{abc}\,[\mathrm{V}]^3$ (coming from the current PI controllers), the pulse width modulation (PWM) generates the corresponding switching patterns $\mathbf{s}_{g}^{abc}\,[1]^3$ for the converter. To estimate angle $\phi_g\,[\mathrm{rad}]$, angular velocity $\omega_g\,[\mathrm{rad/s}]$ and amplitude $\widehat{u}_g\,[\mathrm{V}]$ of the three-phase grid voltage $\mathbf{u}_{g}^{abc}\,[\mathrm{V}]^3$, a phase-locked loop (PLL) is implemented (see [9] or [24, Chap. 8]). The angle $\phi_g\,[\mathrm{rad}]$ is required for the grid voltage orientation of the $k=(d,q)$-reference frame. Angular velocity $\omega_g\,[\mathrm{rad/s}]$ and voltage amplitude $\widehat{u}_g$ are needed for the compensation of the cross-coupling (see Eq. (11.6)) in the current control-loops to decouple the $i_f^d\,[\mathrm{A}]$- and $i_f^q\,[\mathrm{A}]$-dynamics.[7] With the Park and Clarke transformation in Eq. (11.1), the three-phase signals are transformed to the $k=(d,q)$-reference frame and vice versa (grid voltage orientation). The current PI controllers are tuned according to the *Magnitude Optimum* which, with current decoupling feedforward control, allows to approximate the current control-loop dynamics by Eq. (11.3) (see [9] and Assumption (A.3)). Implementation and system data is collected in Table 11.1.

[7] Note that an ideal decoupling is not feasible e.g. due to delays and non-causal compensation terms. For details see [9].

description	symbols & values (with unit)
Implementation data in Matlab/Simulink	
solver (fixed step)	ode4 (Runge-Kutta)
fixed-step size	$h = 2 \times 10^{-6}\,\mathrm{s}$ (fundamental sample time)
System data	
grid	$\widehat{u}_g = 250\,\mathrm{V}$, $\omega_g = 2\pi 50\,\frac{\mathrm{rad}}{\mathrm{s}}$ (balanced)
filter	$R_f = 5 \times 10^{-3}\,\Omega$, $L_f = 3.6 \times 10^{-3}\,\mathrm{H}$
converter	$f_{\mathrm{pwm}} = 8 \times 10^{3}\,\mathrm{Hz}$, $C_{\mathrm{dc}} = 400 \times 10^{-6}\,\mathrm{F}$
	$u_{\mathrm{dc,min}} = 500\,\mathrm{V}$, $u_{\mathrm{dc,max}} = 800\,\mathrm{V}$
current control	$T_{\mathrm{app}} = 1.25 \times 10^{-4}\,\mathrm{s}$ (implementation as in [9])
	$i_{f,\mathrm{min}}^{d} = -277\,\mathrm{A}$, $i_{f,\mathrm{max}}^{d} = +275\,\mathrm{A}$
Controller design data	
classical PI (11.27)	$V_R = \varepsilon_V V_{R,\mathrm{max}}$ as in (11.43), $T_n = \varepsilon_T T_{n,\mathrm{min}}$ as in (11.46)
	with $\varepsilon_V = 0.8$ and $\varepsilon_T = 1.25$
nonlinear PI (11.47)	$V_R(i_f^d, u_{\mathrm{dc}})$ as in (11.60), $T_n(i_f^d)$ as in (11.61)
	with $\lambda_I = -200\,\frac{\mathrm{rad}}{\mathrm{s}}$ and $\lambda_R = -450\,\frac{\mathrm{rad}}{\mathrm{s}}$

Table 11.1 Implementation, system, and controller design data (if not stated otherwise)

The classical DC-link PI controller in Eq. (11.27) is implemented in state space. The controller parameters are listed in Table 11.1. The factors $\varepsilon_V = 0.8$ and $\varepsilon_T = 1.25$ are the stability margins as introduced in Eq. (11.43) and in Eq. (11.46), respectively (see Fig. 11.5).

The nonlinear DC-link PI controller is implemented as in Eq. (11.47). Its varying gains as in Eq. (11.60) and in Eq. (11.61) are adjusted online with respect to the actual measurements of $i_f^d(t)$ and $u_{\mathrm{dc}}(t)$. For "online pole placement", the desired poles were chosen as listed in Table 11.1.

Remark 11.6. In stand-alone operation of the airborne wind energy system (AWES), the AWES usually operates as voltage source (not as current source as described above). Therefore, the grid-side voltage source inverter comes with an LC-filter and the filter output voltage is controlled by an outer control loop. In this case, the DC-link controller must be implemented on the machine side. DC-link controller design on machine side is slightly more complex (due to the nonlinearity of the machine and the aerodynamical torque) but, in principle, very similar to the presented results; in particular, the possible non-minimum phase behavior of the DC-link dynamics remains and imposes the most severe challenge to controller design and stability.

11.6.2 Simulation Experiments

To illustrate and evaluate the control performance of classical and nonlinear DC-link PI controller, *four* simulation experiments are implemented in Matlab/Simulink:

(E_1) Comparison of the control performance of the classical PI controller in Eq. (11.27) and the nonlinear PI controller in Eq. (11.47) for decreasing values of the DC-link capacitance $C_{dc} \in \{800 \times 10^{-6}\,\mathrm{F}, 600 \times 10^{-6}\,\mathrm{F}, 400 \times 10^{-6}\,\mathrm{F}\}$ (see Fig. 11.8).

(E_2) Disturbance rejection capability of the nonlinear PI controller given in Eq. (11.47) *under parameter uncertainties*:

- $\pm 30\%$ parameter uncertainty in the DC-link capacitance C_{dc} (see Fig. 11.9),
- $\pm 30\%$ parameter uncertainty in filter resistance R_f (see Fig. 11.10), and
- $\pm 30\%$ parameter uncertainty in filter inductance L_f (see Fig. 11.11).

(E_3) Set-point tracking performance of the nonlinear PI controller in Eq. (11.47) *under parameter uncertainties*:

- $\pm 30\%$ parameter uncertainty in the DC-link capacitance C_{dc} (see Fig. 11.12),
- $\pm 30\%$ parameter uncertainty in filter resistance R_f (see Fig. 11.13), and
- $\pm 30\%$ parameter uncertainty in filter inductance L_f (see Fig. 11.14).

(E_4) Control performance of the nonlinear PI controller in Eq. (11.47) *for a real (measured) machine power flow* (see Fig. 11.15).

11.6.2.1 Discussion of Experiment (E_1)

Experiment (E_1) compares the disturbance rejection capabilities of the *classical* and *nonlinear* DC-link PI controllers. The simulation results for the experiment are depicted in Fig. 11.8. The following signals are shown: machine power p_m (with changing sign acting as disturbance, see first sub-plot) and the DC-link voltage u_{dc} for three different values of the DC-link capacitor $C_{dc} = 800 \times 10^{-6}\,\mathrm{F}$ (see second sub-plot), $C_{dc} = 600 \times 10^{-6}\,\mathrm{F}$ (see third sub-plot) and $C_{dc} = 400 \times 10^{-6}\,\mathrm{F}$ (see fourth sub-plot). For all three values of C_{dc}, the control performance of the *nonlinear* PI controller is superior to the *classical* PI controller. Its disturbance rejection capability is (much) faster and exhibits (much) smaller under-/overshoots after a step-like change of the machine power. Although the classical PI controller is re-tuned for each value of C_{dc}, for $C_{dc} = 400 \times 10^{-6}\,\mathrm{F}$, it is no longer capable to stabilize the closed-loop system. It becomes unstable after 0.2 s, whereas the *nonlinear* PI controller is able to compensate for the rapid changes in the machine power for all three capacitances. The online adjustment of the controller parameters results in a faster and more accurate disturbance rejection even for the smallest DC-link capacitance $C_{dc} = 400 \times 10^{-6}\,\mathrm{F}$.

Remark 11.7. Due to the *unstable* closed-loop system behavior for the capacitance $C_{dc} = 400 \times 10^{-6}\,\mathrm{F}$, the *classical* PI controller will *no longer* be considered. In the upcoming experiments, *solely* the smallest DC-link capacitance $C_{dc} = 400 \times 10^{-6}\,\mathrm{F}$ will be used.

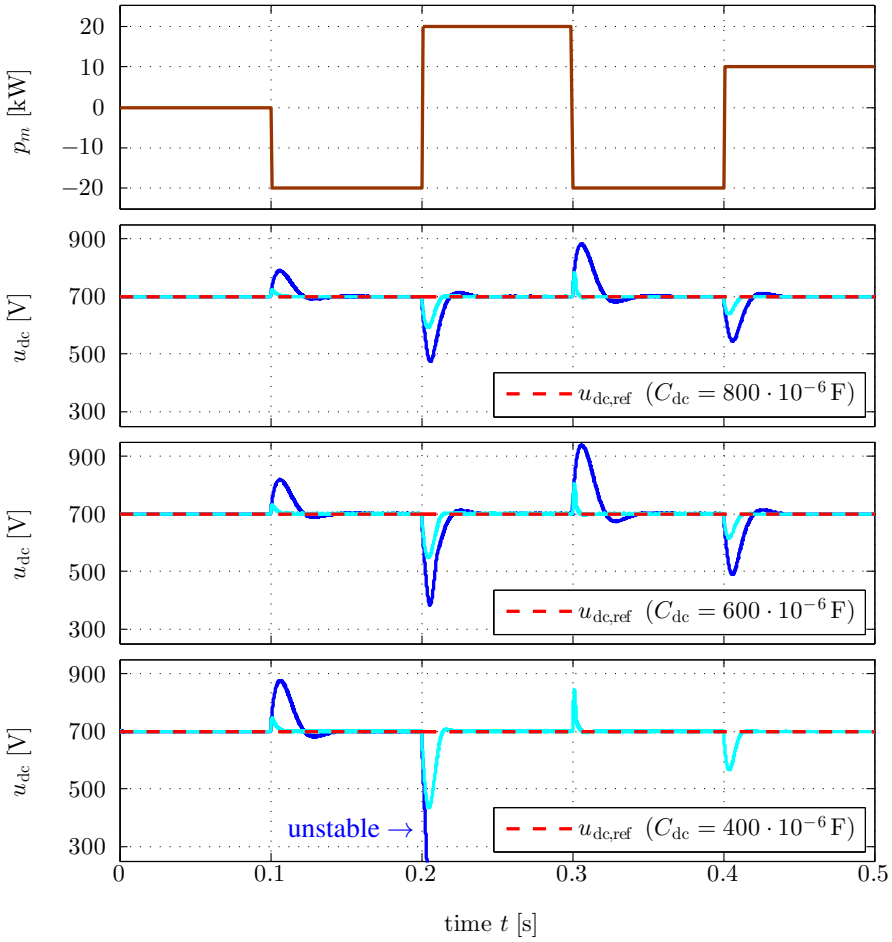

Fig. 11.8 Comparison of the control performance of the — classical PI controller in Eq. (11.27) and the — nonlinear PI controller in Eq. (11.47) for decreasing values of the DC-link capacitance: $C_{dc} = 800 \times 10^{-6}\,\mathrm{F}$ (second sub-plot), $C_{dc} = 600 \times 10^{-6}\,\mathrm{F}$ (third sub-plot) and $C_{dc} = 400 \times 10^{-6}\,\mathrm{F}$ (fourth sub-plot). The classical PI controller is tuned for each value of C_{dc} separately

11.6.2.2 Discussion of Experiment (E_2)

Experiment (E_2) investigates the disturbance rejection capability of the *nonlinear* PI controller under $\pm 30\,\%$ parameter uncertainties in DC-link capacitance, filter resistance and filter inductance for step-like changes in machine power p_m and reactive power q_{pcc} (both act as disturbances on the DC-link dynamics). The parameter uncertainties are implemented in such a way that the nonlinear PI controller parameters in Eq. (11.60) and in Eq. (11.61) use the (estimated) values C_{dc}, R_f and L_f whereas the physical system is modeled with the "real" values given by

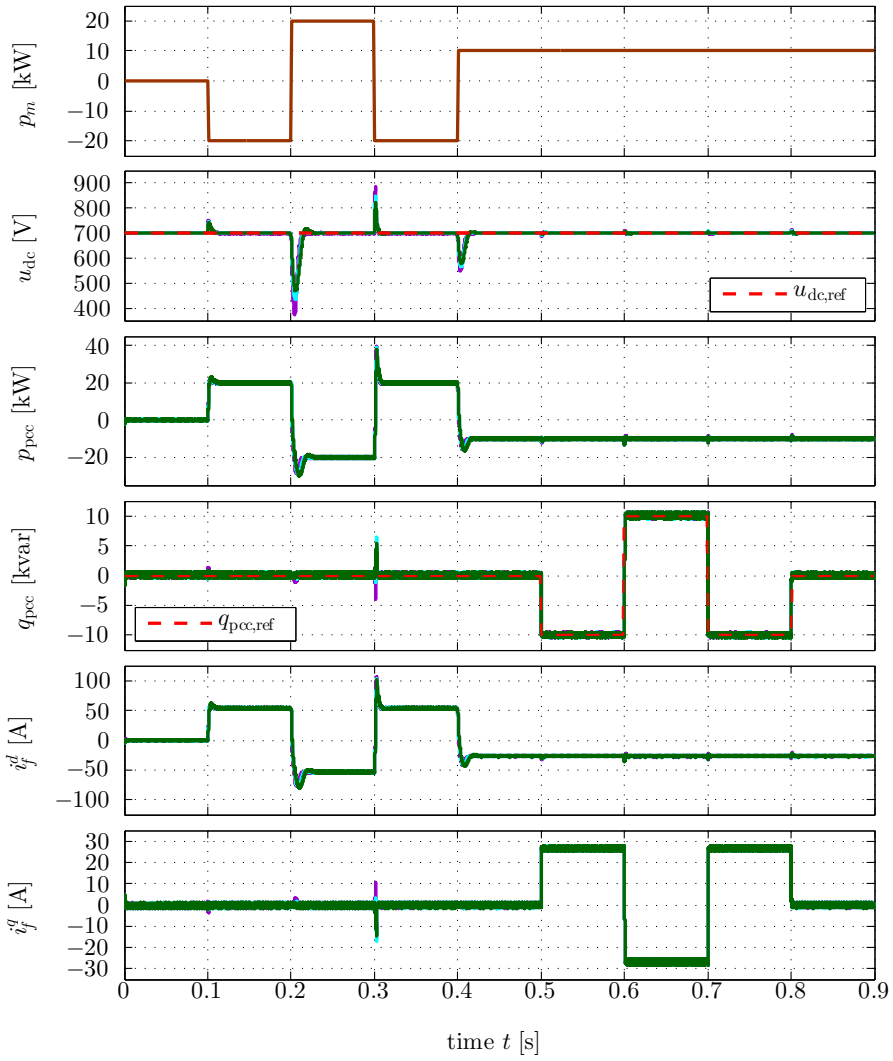

Fig. 11.9 Disturbance rejection of nonlinear DC-link PI controller in Eq. (11.47) for ±30% uncertainties in the DC-link capacitance $C_{\mathrm{dc,real}} = \gamma C_{\mathrm{dc}}$ where $\gamma = 0.7$, $\gamma = 1.0$, $\gamma = 1.3$

$C_{\mathrm{dc,real}} = \gamma C_{\mathrm{dc}}$, $R_{f,\mathrm{real}} = \gamma R_f$ and $L_{f,\mathrm{real}} = \gamma L_f$. The factor $\gamma \in \{0.7, 1, 1.3\}$ is varied. Each value has its own color: $\gamma = 0.7$, $\gamma = 1.0$, $\gamma = 1.3$.

The simulation results for uncertainties in $C_{\mathrm{dc,real}} = \gamma C_{\mathrm{dc}}$, $R_{f,\mathrm{real}} = \gamma R_f$ and $L_{f,\mathrm{real}} = \gamma L_f$ are shown in Fig. 11.9, Fig. 11.10 and Fig. 11.11, respectively. The depicted signals are (from top to bottom) machine power p_m, DC-link voltage u_{dc}, electrical power p_{pcc} at the point of common coupling (PCC), reactive power q_{pcc} at the PCC, and filter currents i_f^d and i_f^q.

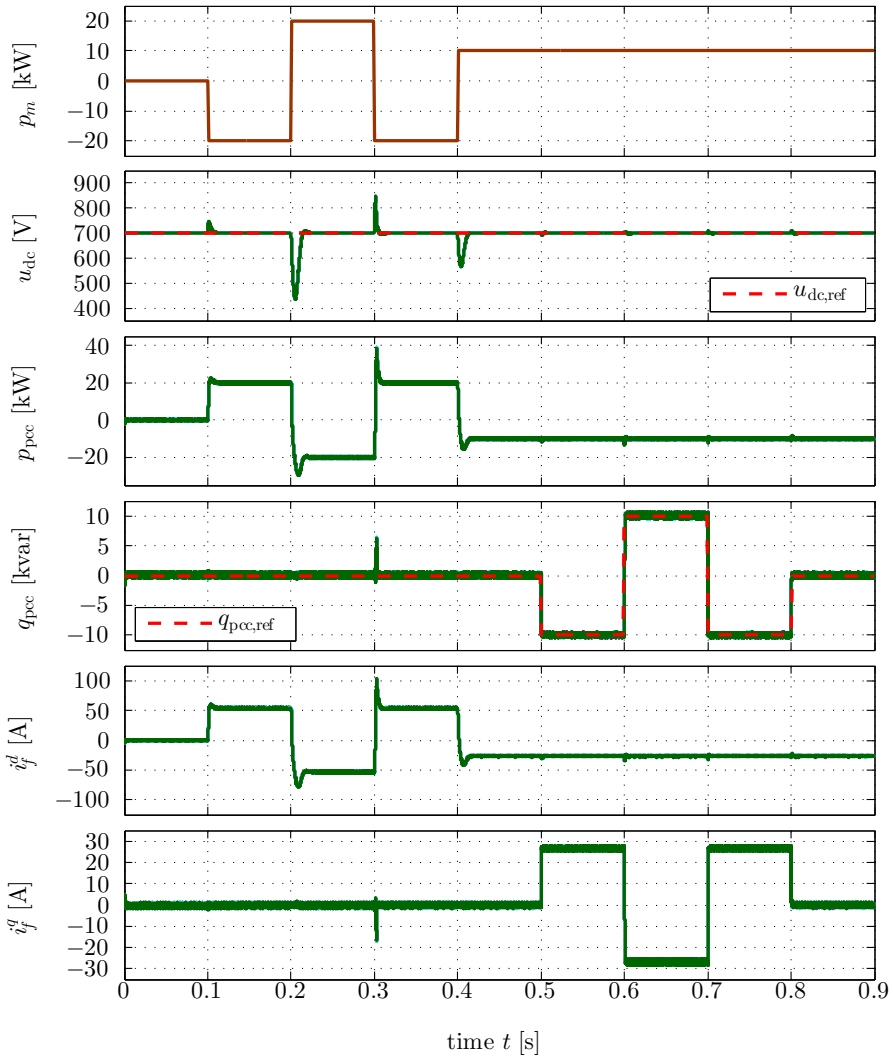

Fig. 11.10 Disturbance rejection of nonlinear DC-link PI controller in Eq. (11.47) for ±30% uncertainties in the filter resistance $R_{f,\mathrm{real}} = \gamma R_f$ where $\gamma = 0.7$, $\gamma = 1.0$, $\gamma = 1.3$

The nonlinear PI controller performs well for all three cases. The closed-loop system remains stable. The disturbances are rejected quickly. The step-like changes in the reactive power have (almost) no effect on the DC-link voltage. Parameter uncertainties in C_{dc} (see Fig. 11.9) affect the set-point tracking control performance. For the case $C_{\mathrm{dc,real}} = 0.7C_{\mathrm{dc}}$, the DC-link voltage exhibits the largest deviations (over-estimation of the capacitance). The other signals are (almost) not influenced.

Parameter uncertainties in R_f (see Fig. 11.10) are negligible. For the three cases $\gamma \in \{0.7, 1, 1.3\}$, all depicted signals are (almost) identical.

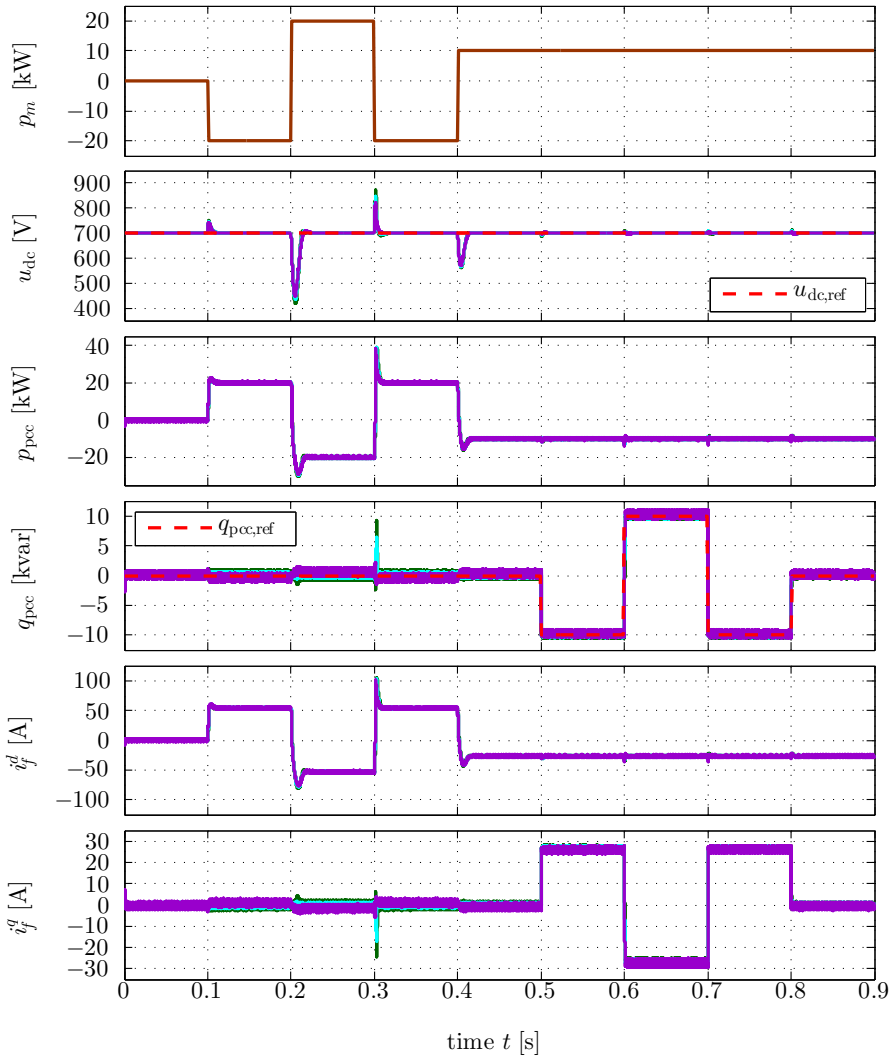

Fig. 11.11 Disturbance rejection of nonlinear DC-link PI controller in Eq. (11.47) for ±30% uncertainties in the filter inductance $L_{f,\mathrm{real}} = \gamma L_f$ where $\gamma = 0.7$, $\gamma = 1.0$, $\gamma = 1.3$

Parameter uncertainties in L_f (see Fig. 11.11) affect the set-point tracking control performances slightly, whereas reactive power and q-component of the current show significant deviations. Here, for $L_{f,\mathrm{real}} = 1.3 L_f$ (under-estimation of the inductance), the largest peaks are visible.

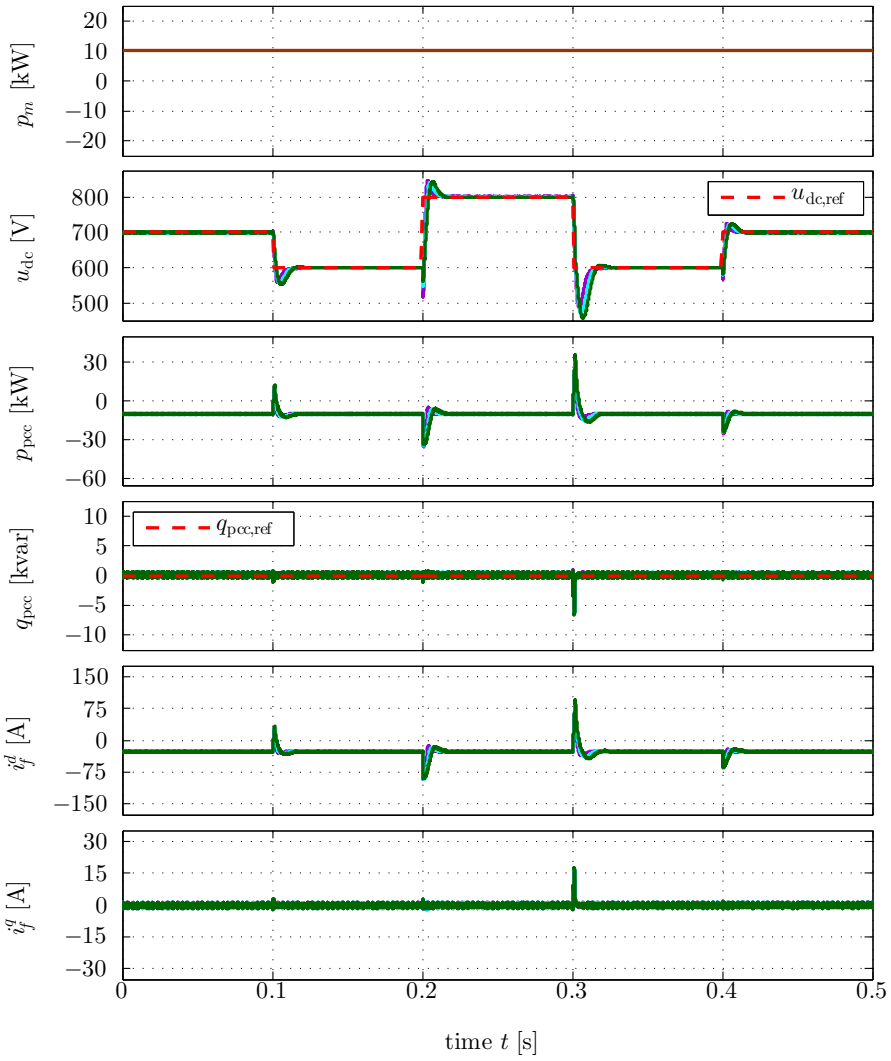

Fig. 11.12 Set-point tracking performance of the nonlinear PI controller in Eq. (11.47) under ±30% uncertainties in the DC-link capacitance $C_{\mathrm{dc,real}} = \gamma C_{\mathrm{dc}}$ where $\gamma = 0.7$, $\gamma = 1.0$, $\gamma = 1.3$

11.6.2.3 Discussion of Experiment (E_3)

Experiment (E_3) illustrates the set-point tracking performance of the *nonlinear* PI controller under $\pm 30\,\%$ parameter uncertainties in C_{dc}, R_f and L_f for a constant but positive machine power (i.e. the non-minimum phase case with $p_m > 0$; motor mode during reel-in phase). The parameter uncertainties are implemented in the identical manner as for Experiment (E_2), i.e. the physical system is modeled with

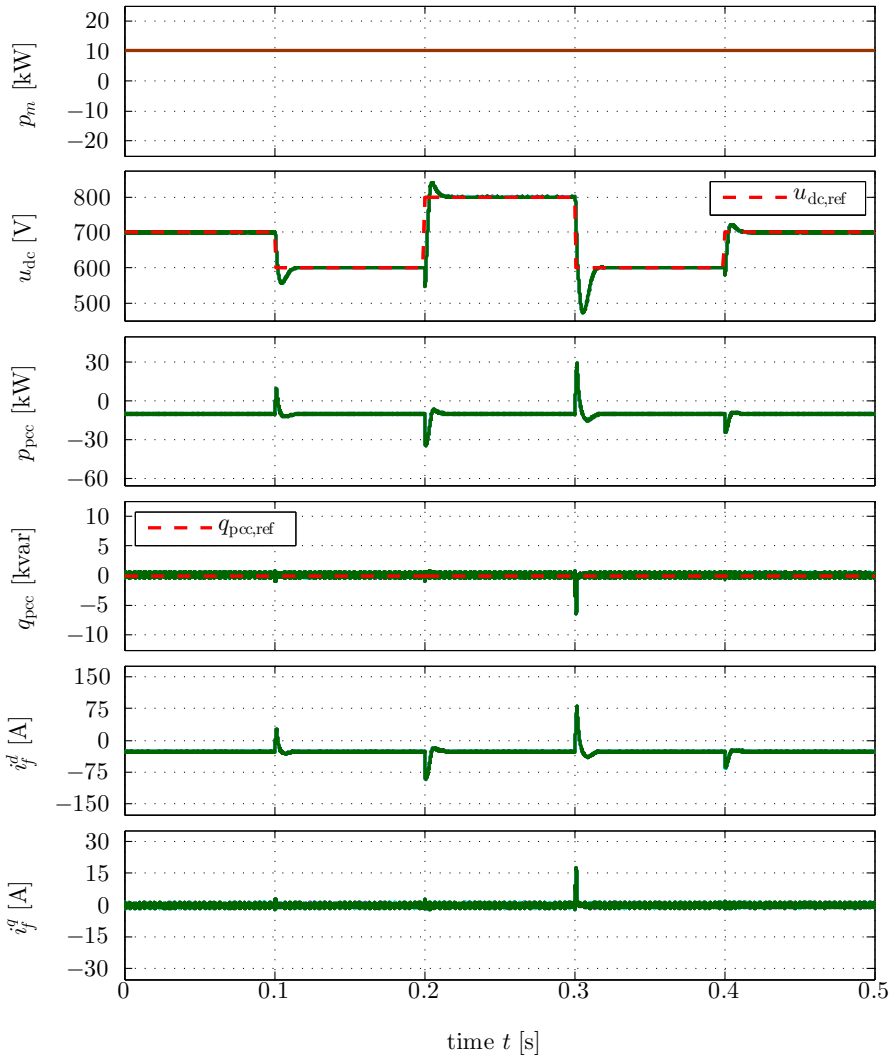

Fig. 11.13 Set-point tracking performance of the nonlinear PI controller in Eq. (11.47) under ±30% uncertainties in the filter resistance $R_{f,\mathrm{real}} = \gamma R_f$ where —— $\gamma = 0.7$, —— $\gamma = 1.0$, —— $\gamma = 1.3$

the "real" values given by $C_{\mathrm{dc,real}} = \gamma C_{\mathrm{dc}}$, $R_{f,\mathrm{real}} = \gamma R_f$ and $L_{f,\mathrm{real}} = \gamma L_f$ where $\gamma \in \{$—— 0.7, —— 1.0, —— 1.3$\}$ is varied. The values of C_{dc}, R_f and L_f are used for controller implementation and tuning.

The simulation results for uncertainties in $C_{\mathrm{dc,real}} = \gamma C_{\mathrm{dc}}$, $R_{f,\mathrm{real}} = \gamma R_f$ and $L_{f,\mathrm{real}} = \gamma L_f$ are shown in Fig. 11.12, Fig. 11.13 and Fig. 11.14, respectively. The plotted signals represent (from top to bottom) machine power p_m, DC-link voltage

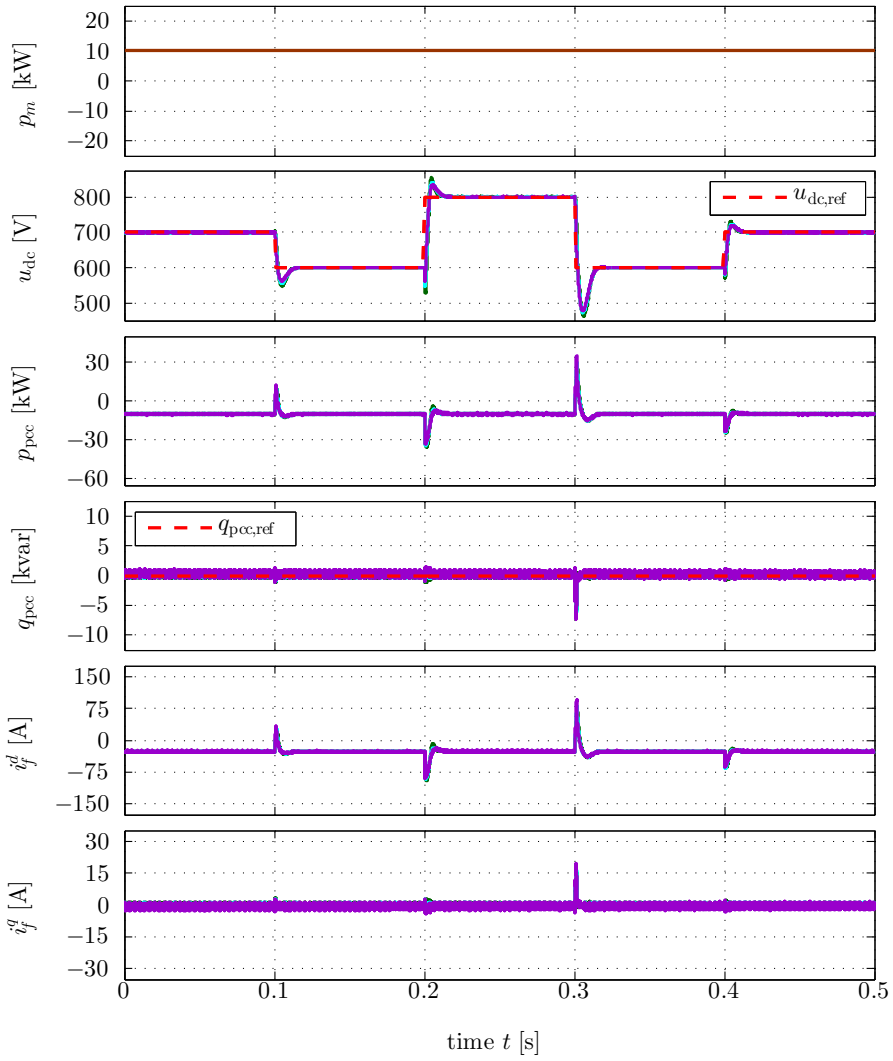

Fig. 11.14 Set-point tracking performance of the nonlinear PI controller in Eq. (11.47) under ±30% uncertainties in the filter inductance $L_{f,\mathrm{real}} = \gamma L_f$ where $\gamma = 0.7$, $\gamma = 1.0$, $\gamma = 1.3$

u_{dc}, electrical power p_{pcc} at the point of common coupling (PCC), reactive power q_{pcc} at the PCC, and filter currents i_f^d and i_f^q.

The set-point tracking performance of the nonlinear PI controller performs is acceptable. Most important, the closed-loop system is stable for all three cases (see Fig. 11.12, Fig. 11.13 and Fig. 11.14). The step-like changes in the reference voltage $u_{\mathrm{dc,ref}}$ are followed quickly with asymptotic accuracy. However, for positive set-point changes at 0.2 s and 0.4 s, the non-minimum phase property of the closed-

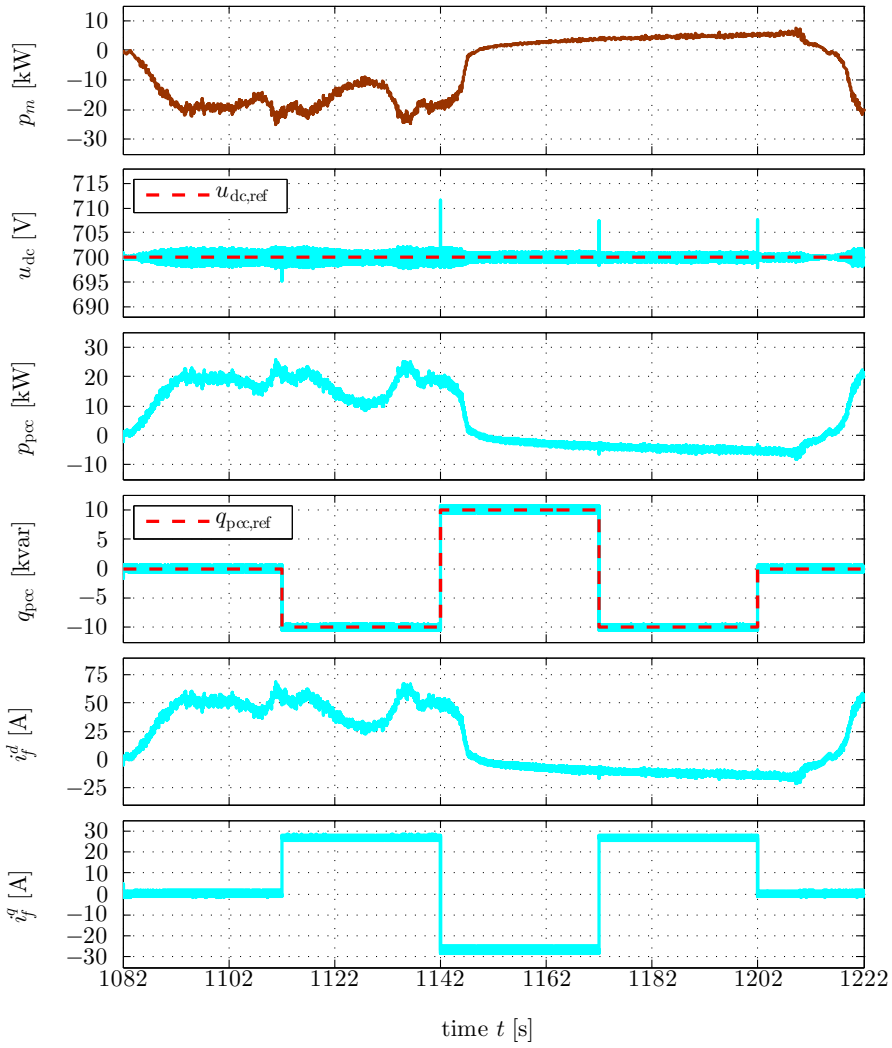

Fig. 11.15 Control performance of the nonlinear PI controller in Eq. (11.47) for a realistic (measured) machine power flow p_m (acting as unfiltered input to the grid-side electrical system)

loop system can be clearly observed: The DC-link voltage u_{dc} decreases before it increases. Moreover, reference changes affect active and reactive power control during transients.

Parameter uncertainties in C_{dc} (see Fig. 11.12), in R_f (see Fig. 11.13) and in L_f (see Fig. 11.14) have only small influence on the set-point tracking performance. Stability is not affected at all.

11.6.2.4 Discussion of Experiment (E_4)

Experiment (E_4) illustrates the control performance of the *nonlinear* PI controller under the most realistic conditions. The utilized machine power p_m was measured by the TU Delft Kite Power group with their demonstrator on 23rd June 2012 (see Fig. 11.2). The simulation results are shown in Fig. 11.15 (from top to bottom): machine power p_m, DC-link voltage u_{dc}, electrical power p_{pcc} at the point of common coupling (PCC), reactive power q_{pcc} at the PCC, filter currents i_f^d and i_f^q.

Both operation modes are simulated: (a) generator mode during the reel-out phase with $p_m(t) < 0$ for $t \in [1\,082\,\mathrm{s}, 1\,150\,\mathrm{s})$ and (b) motor mode during reel-in phase with $p_m(t) > 0$ for $t \in [1\,150\,\mathrm{s}, 1\,218\,\mathrm{s}]$. The DC-link voltage stays within a 2 % band around its reference of $u_{\mathrm{dc,ref}} = 700\,\mathrm{V}$. At 1 142 s, due to the high, step-like change in the reactive power q_{pcc}, the DC-link voltage spikes up to $\approx 712\,\mathrm{V}$ which gives the largest deviation of 12 V from $u_{\mathrm{dc,ref}} = 700\,\mathrm{V}$ (i.e. a relative error of $\approx 1.7\,\%$). Concluding, the nonlinear PI controller achieves a very fast and accurate control performance, also, for real data (measured machine power).

Remark 11.8. Note that the noise in Fig. 11.15 is not due to the online adjustment of the controller gains. The noise is induced by (i) the noisy machine power p_m (see top of Fig. 11.15: the provided measurement data was not filtered and directly used as input to the simulation model) and (ii) the switching behavior of the voltage source inverter which leads to ripples in current and power.

11.7 Conclusion

This chapter discusses two different PI controllers for DC-link voltage control: the classical PI controller with constant parameters and a nonlinear PI controller with online parameter adjustment. DC-link voltage control is a non-trivial task due to the nonlinear and possibly non-minimum phase DC-link dynamics (when power flows from the grid to the DC-link). For both PI controllers, the nonlinear system behavior gives different bounds on the choice of the controller parameters. The bounds are derived based on physical system properties (such as admissible currents and DC-link voltages). A comparison of the controllers shows that the classical PI controller becomes unstable for decreasing DC-link capacitances whereas the nonlinear PI controller remains stable. Moreover, the nonlinear DC-link PI controller is (very) robust to parameter uncertainties in filter resistance, filter inductance and DC-link capacitance. Concluding, the implementation of the nonlinear PI controller, compared to the classical PI controller design, seems promising since it is more robust and stable and allows the installation of smaller capacitances which brings economical benefit.

Nomenclature

$\mathbb{R}, \mathbb{C}$	real, complex numbers.
$\mathbf{x} := (x_1, \ldots, x_n)^\top \in \mathbb{R}^n$	column vector, $n \in \mathbb{N}$ where $^\top$ and $:=$ mean 'transposed' (interchanging rows and columns of matrix or vector) and 'is defined as'.
$\mathbf{0}_n \in \mathbb{R}^n$	zero vector.
$\mathbf{a}^\top \mathbf{b} := a_1 b_1 + \cdots + a_n b_n$	scalar product of the vectors $\mathbf{a} := (a_1, \ldots, a_n)^\top$ and $\mathbf{b} := (b_1, \ldots, b_n)^\top$.
$\|\mathbf{x}\| := \sqrt{\mathbf{x}^\top \mathbf{x}} = \sqrt{x_1^2 + \cdots + x_n^2}$	Euclidean norm of $\mathbf{x}$.
$\mathbf{A} \in \mathbb{R}^{n \times n}$	(square) matrix with n rows and columns.
$\mathbf{A}^{-1}$	inverse of $\mathbf{A}$ (if exists).
$\det(\mathbf{A})$	determinant of $\mathbf{A}$.
$\operatorname{spec}(\mathbf{A})$	spectrum of $\mathbf{A}$ (eigenvalues of $\mathbf{A}$).
$\mathbf{I}_n \in \mathbb{R}^{n \times n} := \operatorname{diag}(1, \ldots, 1)$	identity matrix.
$\mathscr{L}^\infty(I; Y)$	space of (essentially) bounded functions with norm $\|\mathbf{f}\|_\infty := \text{ess-sup}_{t \in I} \|\mathbf{f}(t)\|$ (essential supremum). Simple example: For a piecewise continuous function $\mathbf{f}(\cdot) \in \mathscr{L}^\infty(I; Y)$, there exists a positive constant $c_f > 0$, such that $\sup_{t \in I} \|\mathbf{f}(t)\| \leq c_f$ for all $t \in I$. Hence, $\mathbf{f}(\cdot)$ is bounded for all $t \in I$.
$\alpha \overset{(\#)}{=} \beta$	equivalence of α and β follows directly by invoking Eq. (#) (same notation is also used for relations, e.g. $\overset{(\#)}{<}$, $\overset{(\#)}{\leq}$, $\overset{(\#)}{\geq}$ and $\overset{(\#)}{>}$).
$\mathbf{x}\,[\mathrm{X}]^n$	physical quantity $\mathbf{x} \in \mathbb{R}^n$, each of the n elements has SI-unit X.
$\boldsymbol{\xi}^{abc} := \left(\xi^a, \xi^b, \xi^c\right)^\top \in \mathbb{R}^3$	signal $\boldsymbol{\xi}^{abc}$ (may represent currents and voltages, i.e. $\boldsymbol{\xi} \in \{\mathbf{i}, \mathbf{u}\}$) in the three-phase (a,b,c)-reference frame.
$\boldsymbol{\xi}^s := \left(\xi^\alpha, \xi^\beta\right)^\top \in \mathbb{R}^2$	signal $\boldsymbol{\xi}^s$ in the stator-fixed (α,β)-reference frame.
$\boldsymbol{\xi}^k = \left(\xi^d, \xi^q\right)^\top \in \mathbb{R}^2$	signal $\boldsymbol{\xi}^k$ in the arbitrarily rotating $k = (d,q)$-reference frame.

References

1. Ahmed, M. S., Hably, A., Bacha, S.: Kite Generator System Modeling and Grid Integration. IEEE Transactions on Sustainable Energy **4**(4), 968–976 (2013). doi: 10.1109/TSTE.2013.2260364
2. Ahmed, M., Hably, A., Bacha, S., Ovalle, A.: Kite generator system: Grid integration and validation. In: Proceedings of the 40th Annual Conference of the IEEE Industrial Electronics Society (IECON 2014), pp. 2139–2145, Dallas, TX, USA, 29 Oct–1 Nov 2014. doi: 10.1109/IECON.2014.7048798
3. Bauer, F., Hackl, C. M., Schechner, K.: DC-link control for airborne wind energy systems during pumping mode. In: Schmehl, R. (ed.). Book of Abstracts of the International Airborne Wind Energy Conference 2015, p. 60, Delft, The Netherlands, 15–16 June 2015. doi: 10.4233/uuid:7df59b79-2c6b-4e30-bd58-8454f493bb09. Presentation video recording available from: https://collegerama.tudelft.nl/Mediasite/Play/599c28511f704d7898d785f584150fb31d
4. Bode, H. W.: Relations Between Attenuation and Phase in Feedback Amplifier Design. Bell System Technical Journal **19**(3), 421–454 (1940). doi: 10.1002/j.1538-7305.1940.tb00839.x
5. Diehl, M.: Airborne Wind Energy: Basic Concepts and Physical Foundations. In: Ahrens, U., Diehl, M., Schmehl, R. (eds.) Airborne Wind Energy, Green Energy and Technology, Chap. 1, pp. 3–22. Springer, Berlin Heidelberg (2013). doi: 10.1007/978-3-642-39965-7_1
6. Ding, X., Qian, Z., Yang, S., Cui, B., Peng, F.: A direct DC-link boost voltage PID-like fuzzy control strategy in Z-source inverter. In: Proceedings of the IEEE Power Electronics Specialists Conference, pp. 405–411, Rhodes, Greece, 15–19 June 2008. doi: 10.1109/PESC.2008.4591963
7. Dirscherl, C., Hackl, C. M., Schechner, K.: Pole-placement based nonlinear state-feedback control of the DC-link voltage in grid-connected voltage source power converters: A preliminary study. In: Proceedings of the 2015 IEEE Conference on Control Applications (CCA), pp. 207–214, Sydney, Australia, 21–23 Sept 2015. doi: 10.1109/CCA.2015.7320634
8. Dirscherl, C., Hackl, C., Schechner, K.: Explicit model predictive control with disturbance observer for grid-connected voltage source power converters. In: Proceedings of the 2015 IEEE International Conference on Industrial Technology, pp. 999–1006, Seville, Spain, 17–19 Mar 2015. doi: 10.1109/ICIT.2015.7125228
9. Dirscherl, C., Hackl, C., Schechner, K.: Modellierung und Regelung von modernen Windkraftanlagen: Eine Einführung. In: Schröder, D. (ed.) Elektrische Antriebe – Regelung von Antriebssystemen, Chap. 24, pp. 1540–1614. Springer, Berlin Heidelberg (2015). doi: 10.1007/978-3-642-30096-7_24
10. Fagiano, L., Milanese, M.: Airborne Wind Energy: an overview. In: Proceedings of the 2012 American Control Conference, pp. 3132–3143, Montréal, QC, Canada, 27–29 June 2012. doi: 10.1109/ACC.2012.6314801
11. Gensior, A., Sira-Ramirez, H., Rudolph, J., Guldner, H.: On Some Nonlinear Current Controllers for Three-Phase Boost Rectifiers. IEEE Transactions on Industrial Electronics **56**(2), 360–370 (2009). doi: 10.1109/TIE.2008.2003370
12. Heidary Yazdi, S., Fathi, S., Gharehpetian, G., Ma'ali Amiri, E.: Regulation of DC link voltage in VSC-HVDC to prevent DC voltage instability based on accurate dynamic model. In: Proceedings of the 4th Power Electronics, Drive Systems and Technologies Conference, pp. 394–400, Tehran, Iran, 13–14 Feb 2013. doi: 10.1109/PEDSTC.2013.6506740
13. Hinrichsen, D., Pritchard, A. J.: Mathematical Systems Theory I – Modelling, State Space Analysis, Stability and Robustness. Texts in Applied Mathematics, vol. 48. Springer-Verlag, Berlin Heidelberg (2005). doi: 10.1007/b137541
14. Loyd, M. L.: Crosswind kite power. Journal of Energy **4**(3), 106–111 (1980). doi: 10.2514/3.48021
15. Muslem Uddin, S. M., Akter, P., Mekhilef, S., Mubin, M., Rivera, M., Rodriguez, J.: Model predictive control of an active front end rectifier with unity displacement factor. In: Proceed-

ings of the 2013 IEEE International Conference on Circuits and Systems, pp. 81–85, Kuala Lumpur, Malaysia, 18–19 Sept 2013. doi: 10.1109/CircuitsAndSystems.2013.6671612
16. Olalla, C., Leyva, R., El Aroudi, A., Queinnec, I.: LMI control applied to non-minimum phase switched power converters. In: Proceedings of the IEEE International Symposium on Industrial Electronics, pp. 154–159, Cambridge, United Kingdom, 30 June–2 July 2008. doi: 10.1109/ISIE.2008.4676993
17. Pérez, M. A., Fuentes, R., Rodríguez, J.: Predictive control of DC-link voltage in an active-front-end rectifier. In: Proceedings of the 2011 IEEE International Symposium on Industrial Electronics, pp. 1811–1816, Gdansk, Poland, 27–30 June 2011. doi: 10.1109/ISIE.2011.5984432
18. Rodriguez, H., Ortega, R., Escobar, G.: A robustly stable output feedback saturated controller for the Boost DC-to-DC converter. In: Proceedings of the 38th IEEE Conference on Decision and Control, vol. 3, pp. 2100–2105, Phoenix, AZ, USA, 7–10 Dec 1999. doi: 10.1109/CDC.1999.831229
19. Schröder, D.: Elektrische Antriebe - Regelung von Antriebssystemen. 3rd ed. Springer, Berlin Heidelberg (2009). doi: 10.1007/978-3-540-89613-5
20. Schröder, D.: Leistungselektronische Schaltungen: Funktion, Auslegung und Anwendung. Springer-Verlag, Berlin Heidelberg (2012). doi: 10.1007/978-3-642-30104-9
21. Shukla, A., Ghosh, A., Joshi, A.: State Feedback Control of Multilevel Inverters for DSTATCOM Applications. IEEE Transactions on Power Delivery **22**(4), 2409–2418 (2007). doi: 10.1109/TPWRD.2007.905271
22. Song, E., Lynch, A., Dinavahi, V.: Experimental Validation of Nonlinear Control for a Voltage Source Converter. IEEE Transactions on Control Systems Technology **17**(5), 1135–1144 (2009). doi: 10.1109/TCST.2008.2001741
23. Sosa, J. M., Martínez-Rodríguez, P. R., Vázquez, G., Nava-Cruz, J. C.: Control design of a cascade boost converter based on the averaged model. In: Proceedings of the 2013 IEEE International Autumn Meeting on Power, Electronics and Computing, pp. 1–6, Morelia, Michoacán, Mexico, 13–15 Nov 2013. doi: 10.1109/ROPEC.2013.6702718
24. Teodorescu, R., Liserre, M., Rodríguez, P.: Grid Converters for Photovoltaic and Wind Power Systems. John Wiley & Sons, Ltd., Chichester, United Kingdom (2011)
25. Thakur, R. K.: Analysis and control of a variable speed wind turbine drive system dynamics. In: Proceedings of the International Conference on Power Systems, pp. 1–5, Kharagpur, India, 27–29 Dec 2009. doi: 10.1109/ICPWS.2009.5458447
26. Vasiladiotis, M., Rufer, A.: Dynamic Analysis and State Feedback Voltage Control of Single-Phase Active Rectifiers With DC-Link Resonant Filters. IEEE Transactions on Power Electronics **29**(10), 5620–5633 (2014). doi: 10.1109/TPEL.2013.2294909
27. Wen-Lei, L.: Adaptive dynamic surface tracking control for DC-DC boost converter. In: Proceedings of the 31st Chinese Control Conference, pp. 750–755, Hefei, China, 25–27 July 2012
28. Yaramasu, V., Wu, B.: Predictive Control of a Three-Level Boost Converter and an NPC Inverter for High-Power PMSG-Based Medium Voltage Wind Energy Conversion Systems. IEEE Transactions on Power Electronics **29**(10), 5308–5322 (2014). doi: 10.1109/TPEL.2013.2292068
29. Zhang, L., Nee, H.-P., Harnefors, L.: Analysis of Stability Limitations of a VSC-HVDC Link Using Power-Synchronization Control. IEEE Transactions on Power Systems **26**(3), 1326–1337 (2011). doi: 10.1109/TPWRS.2010.2085052
30. Zhang, Y., Liu, J., Ma, X., Feng, J.: Model and control of diode-assisted buck-boost voltage source inverter. In: Proceedings of the 1st International Future Energy Electronics Conference, pp. 734–739, Tainan, Taiwan, 3–6 Nov 2013. doi: 10.1109/IFEEC.2013.6687599
31. Zhang, Y., Liu, J., Ma, X., Feng, J.: Multi-loop controller design for diode-assisted buck-boost voltage source inverter. In: Proceedings of the 2014 International Power Electronics Conference, pp. 835–842, Hiroshima, Japan, 18–21 May 2014. doi: 10.1109/IPEC.2014.6869685